To appear in the September 2006 issue of PASP

Evaluation of the ALMA Prototype Antennas[1]

Jeffrey G. Mangum

National Radio Astronomy Observatory, 520 Edgemont Road, Charlottesville, VA 22903, USA

jmangum@nrao.edu

Jacob W. M. Baars

Max-Planck-Institut für Radioastronomie, Auf dem Hügel 69, D-53121 Bonn, Germany and European Southern Observatory, D-85748 Garching, Germany

jacobbaars@arcor.de

Albert Greve

Institut de Radio Astronomie Millimétrique, 300 rue de la Piscine, Domaine Universitaire, 38406 Saint Martin d'Héres, France

greve@iram.fr

Robert Lucas

Institut de Radio Astronomie Millimétrique, 300 rue de la Piscine, Domaine Universitaire, 38406 Saint Martin d'Héres, France

lucas@iram.fr

Ralph C. Snel

SRON Netherlands Institute for Space Research, Sorbonnelaan 2, 3584 CA UTRECHT, The Netherlands

R.Snel@sron.nl

Patrick Wallace

Rutherford Appleton Laboratory, Chilton, Didcot, Oxon OX11 0QX, UK

ptw@star.rl.ac.uk

and

Mark Holdaway

National Radio Astronomy Observatory, 949 North Cherry Avenue, Tucson, AZ 85721, USA

mholdawa@nrao.edu

ABSTRACT

The ALMA North American and European prototype antennas have been evaluated by a variety of measurement systems to quantify the major performance specifications. Nearfield holography was used to set the reflector surfaces to 17 μm RMS. Pointing and fast switching performance was determined with an optical telescope and by millimeter wavelength radiometry, yielding 2″ absolute and 0.6″ offset pointing accuracies. Path length stability was measured to be $\lesssim$ 20 μm over 10 minute time periods using optical measurement devices. Dynamical performance was studied with a set of accelerometers, providing data on wind induced tracking errors and structural deformation. Considering all measurements made during this evaluation, both prototype antennas meet the major ALMA antenna performance specifications.

1. Introduction

In the early stages of the collaboration between the National Radio Astronomy Observatory (NRAO) and the European Southern Observatory (ESO) toward the joint design, construction and operation of a large millimeter array (now called the Atacama Large Millimeter Array, or "ALMA", project), it was agreed that each of the partners would acquire from industry a prototype of the planned 12 m diameter antennas. The specifications of these antennas are beyond the current state of the art in accurate reflector antenna technology. Considering that 64 of these antennas would eventually be needed, this step appeared warranted to mitigate performance risk and increase competition among prospective manufacturers. It was also agreed to place the antennas next to each other at a suitable site

[1]The performance results presented in this publication were part of a comprehensive technical evaluation process used to evaluate the ALMA prototype antennas which concluded in April 2005.

and subject them to an extensive evaluation program to be carried out by a joint team of scientists and engineers drawn from the institutes of the ALMA collaboration.

The two ALMA prototype antennas are located at the site of the Very Large Array (VLA) in New Mexico. This site provides a reasonable compromise between the quality of the atmosphere, necessary for millimeter wavelength operation, and ease of construction and operation. The latter is provided by the existing infrastructure of the VLA site. The atmospheric characteristics however allow only operation at relatively long millimeter wavelengths during the dry winter months. Thus, the antennas have been equipped with evaluation receivers for the wavelength bands near 3 and 1.2 mm.

The evaluation of the antennas has been carried out by the Antenna Evaluation Group (AEG), consisting of experienced "antenna integrators and commissioners" from both organizations, Associated Universities Incorporated (AUI)/National Radio Astronomy Observatory (NRAO) and the European Southern Observatory (ESO). The charge of the AEG was to subject both antennas to a series of identical tests that would indicate the compliance (or not) of the antennas with the specifications. The core of the AEG is composed of the authors of this paper.

2. Description of the Prototype Antennas

The ALMA prototype antennas are alt-azimuth mounted Cassegrain reflector systems of 12 m diameter with a reflector surface and pointing accuracy suitable for observations in the 0.3 mm submillimeter band. VertexRSI delivered an antenna to AUI/NRAO (see Figure 1) and ESO obtained an antenna from the consortium Alcatel/EIE (AEC; see Figure 2). The main characteristics of the antennas are summarized in Table 1.

The two antennas show interesting differences. To minimise the structural deformations due to temperature changes, both make extensive use of carbon-fiber reinforced-plastic (CFRP) for the back-up structure (BUS) of the reflector. The BUS is a box-structure, thus avoiding the need to design and fabricate the intricate joints of a space-frame structure in CFRP. The AEC group has realised the entire elevation structure (receiver cabin and connection to BUS) in CFRP, while VertexRSI applies insulated steel for the cabin and Invar for the connection cone to the BUS. For the drive systems, VertexRSI uses a traditional pinion and gear rack system, while AEC uses a direct linear drive, applied for instance in the Very Large Telescope (VLT) optical telescopes or the Berkeley Illinois Maryland Association (BIMA) antennas.

There are significant differences in the choice of size and technology of the reflector

Fig. 1.— The VertexRSI ALMA prototype antenna.

Fig. 2.— The AEC ALMA prototype antenna.

Table 1: Main Properties of the ALMA Prototype Antennas

Property	**VertexRSI**	**Alcatel/EIE (AEC)**
Base/Yoke/Cabin	Insulated Steel	Insulated Steel/Insulated Steel/ CFRP
BUS	Al honeycomb with CFRP plating, 24 sectors, open back, covered by removable GFRP[a] sunshades	Solid CFRP plates, 16 sectors, closed back sectors glued and bolted together.
Receiver Cabin	Cylindrical; Invar/Thermally-Stabilized Steel	CFRP; Direct connection cabin to BUS
Base	3-point support - bolt connection with foundation	6-point base support - flanged attachments with foundation
Drive	Gear and Pinion	Direct drives on both axes with linear motors
Brakes	Integrated on servo motor	Hydraulic disk brakes
Encoders	Absolute (BEI)	Incremental (Heidenhain)
Panels	264 Panels, 8 rings, machined Al, open back, 8 adjusters (3 lateral/5 axial) per panel	120 Panels, 5 rings. Al-honeycomb core with replicated Ni skins, Rh coated. 5 adjusters per panel
Apex/Quadripod	CFRP structure, + configuration	CFRP structure , × configuration
Focus Mechanism	Hexapod (5 DOF)	Three axes (x,y,z) mechanism
Total Mass	$\sim$ 108 tonnes	$\sim$ 80 tonnes
Mass Dist (El/Az)	50%/50%	35%/65%

[a]Glass Fiber Reinforced Plastic.

panels. The VertexRSI antenna has relatively small panels, made of machined aluminum and chemically etched to achieve the required effective scattering of solar heat radiation. They have separate axial (5) and lateral (3) adjustable supports. The AEC panels are of a novel design by Media Lario. Electroformed nickel skins, replicated from a machined steel mold, are bonded to a 20 mm thick aluminum honeycomb core. To improve the thermal behaviour under sunlight, the surface is coated with 200 nm of rhodium. These larger panels have 5 adjustable axial supports, which also provide sufficient stiffness in the lateral direction. Because of the more extensive use of the relatively lightweight CFRP, the AEC antenna is significantly lighter than the VertexRSI antenna.

3. Major Specifications

The ALMA antennas will be used to a shortest wavelength of about 0.3 mm while located at 5000 m altitude in Chile under rather extreme conditions of strong wind and sunshine. Consequently, the requirements on the accuracy and stability of the reflector surface contour and of the pointing and tracking behaviour are very high. In fact, no radio telescope of comparable size has been designed to the specifications listed below.

It has been the main task of the AEG to establish the compliance of the ALMA prototype antennas with the major performance specifications (see Table 2).

These specifications must be satisfied under all attitude angles of the antenna and all environmental conditions, in particular wind of 6 m/s (day) and 9 m/s (night), as well as full solar illumination from changing directions.

Because of the interferometric mode of operation of ALMA, some unusual specifications have been introduced, such as path length variations and the capability of very fast switching between two relatively close points on the sky. It is beyond the scope of this paper to elaborate on the reasons for these specifications.

4. Evaluation Results

The major performance specifications, results, and the primary operating conditions during which these specifications apply, for the ALMA prototype antennas are listed in Table 2. In the following we describe how the performance of the ALMA prototype antennas was derived within the context of each performance specification. The technical details that describe the various measurement systems and techniques used to derive these results can be found in Mangum et al. (2004), Baars et al. (2006), Greve & Mangum (2006), Holdaway

et. al. (2004), Snel et al. (2006), Wallace et al. (2004), Mangum & Greve (2004), and Mangum (2004). In the following we describe the measurements which lead to the summary results listed in Table 2.

Table 2: Prototype Antenna Specifications and Performance Overview

Property	Specification	Performance	
		VertexRSI	AEC
Surface Accuracy	25 μm RMS with 20 μm RMS goal	16 ± 5 μm	17 ± 5 μm
Absolute Pointing	2 arcsec over all sky	1.3–1.8 arcsec	2.0–2.6 arcsec
Offset Pointing	0.6 arcsec over 2 degrees radius	0.3–1.1 arcsec	0.3–0.8 arcsec
Fast Switching	1.5 degree move in 1.5 seconds, settle to 3 arcsec peak pointing error	1.5–1.8 seconds	1.4–1.8 seconds
Path Length Stability	15/20 μm (Nonrepeatable/Repeatable)	$\leq$(15,21,32) μm[a]	$\leq$(15,18,30) μm[a]
Primary Operating Conditions: $-20\ C \leq T_{amb} \leq +20\ C$; $\Delta T_{amb} \leq$0.6/1.8 C in 10/30 minutes; $V_{wind} \leq$ 6/9 m/s (day/night); Full solar loading			
[a] For Δt< (3,10,30) minutes, respectively.			

5. Reflector Surface Accuracy

5.1. Near-Field Holography Measurements

The near-field holographic method was used to measure and set the surface to an accuracy of better than 20 μm RMS. A transmitter on a 50 m high tower at a distance of 310 m provided the signal at 79 or 104 GHz. See Mangum et al. (2004) and Baars et al. (2006) for further details describing this holographic technique. Figure 3 shows a typical surface error map derived from these holographic measurements.

The holographic measurement and setting of both antennas was performed immediately after the antennas became available for evaluation. During a period of about one year the antennas were subjected to a number of hard loads, like fast switching tests, drive system errors resulting in strong vibrations, and high-speed emergency stops. Also, the influence of wind and diurnal temperature variations on the surface stability was a point of

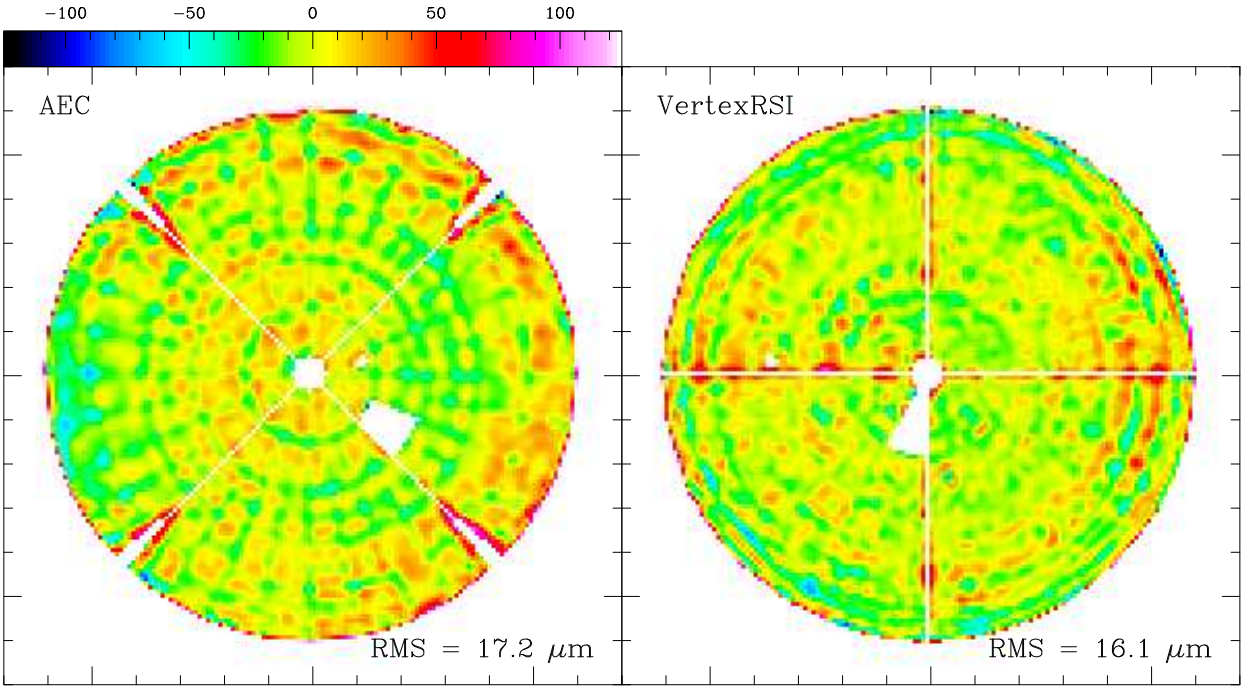

Fig. 3.— Typical final holographic surface map of the AEC (left) and VertexRSI (right) prototype antennas. Note that the "×" (AEC) and "+" (VertexRSI) feed leg structure. The poor measurement results obtained near the feed leg structures of each antenna are due to the difficulties encountered with holographic measurements near these structures.

concern. It was therefore decided to close the evaluation program with a second holographic measurement of the reflector surfaces. This was done in December 2004 to February 2005 during relatively good atmospheric conditions. It was during these measurements that we discovered that we had not properly taken care of a correction explained in Baars et al. (2006). This correction, which did not affect the final interpretation of the prototype antenna surface accuracy performance, was subsequently applied properly. The final surface maps are shown in Figures 4 and 6. Both antennas were set to a surface accuracy of 16–17 μm RMS.

5.1.1. Overview

VertexRSI Antenna: The antenna was delivered with a nominal surface error of 80 μm RMS, as determined from a photogrammetric measurement. Our first holography map showed an RMS of approximately 85 μm. A first setting of the surface resulted in an RMS of 64 μm. In four more steps of holographic measurement followed by adjustment the surface error decreased to 19 μm RMS.

The sequence of surface error maps, along with the RMS and the error distribution, is shown in Figure 4. As allowed in the specification, we have applied a weighting over the aperture proportional to the illumination pattern of the feed. This essentially diminishes the influence of the surface errors in the outer areas of the reflector. The white areas in the surface error maps are the quadripod, optical pointing telescope, and a few bad panels, that could not be set accurately. All of these structures were left out of the calculation of the final overall RMS value.

With increasing accuracy the presence of an artefact in the outer area of the aperture became apparent. There is a "wavy" structure in the outer section with a "period" too large to be inherent in the panels. Experiments with absorbing material showed that it was not caused by multiple reflections. The effect can be described by a DC-offset in the central point of the measured antenna map, *i.e.* some saturation on the point with the highest intensity. By adjusting this offset in the analysis software, most of the artefact could be removed. This has been done with the final data. The additional set of follow-up holography measurements in December 2004 – February 2005 did not suffer from this signal saturation, and no artefact was observed in these follow-up maps. Checks of the holography hardware indeed suggest that the 2003 holography measurements did experience a small amount of signal saturation.

The adjustments were done with a simple tool. Two people on a man-lift approached the surface from the front, where the adjustment screws are located (see Figure 5). The time needed for an adjustment of the total of 1320 adjusters was 8 hours, as required by the

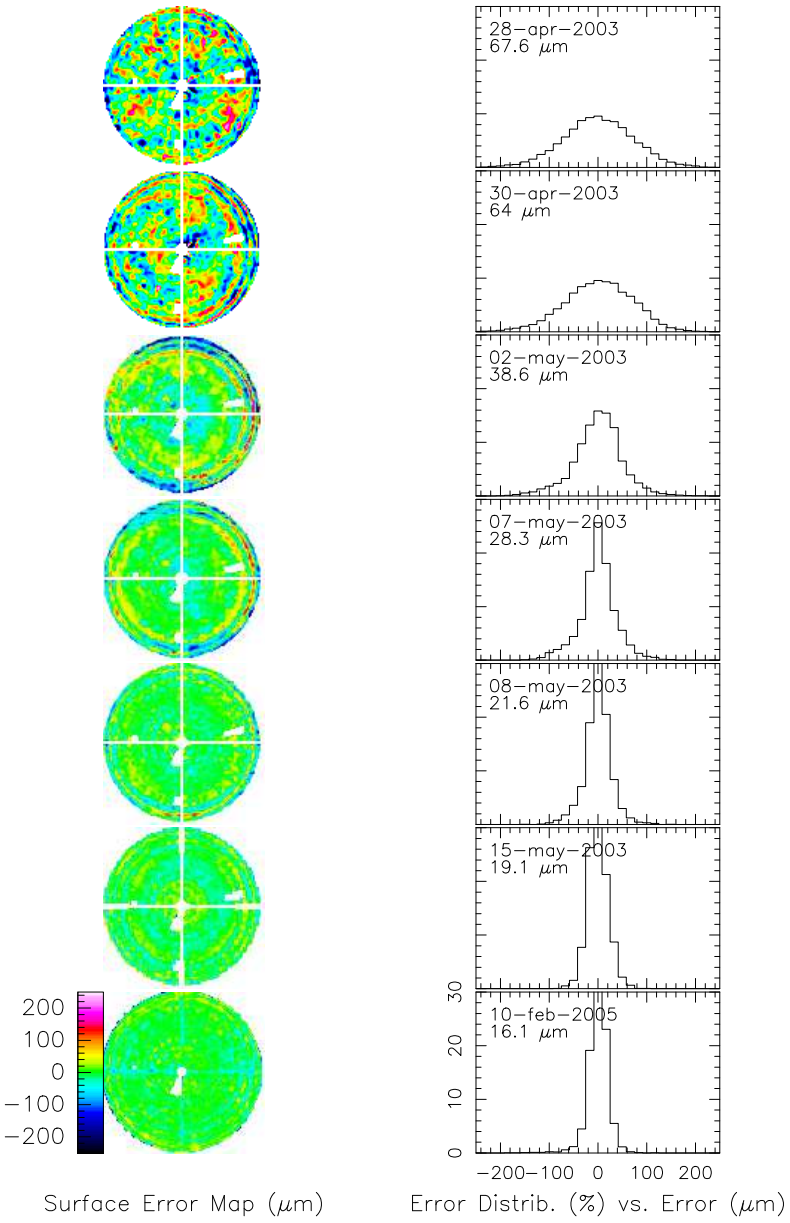

Fig. 4.— Sequence of surface error maps with intermediate panel setting for the VertexRSI antenna. The surface contours are shown on the left side; the error distribution on the right. The white cross and the small white areas represent the quadripod and a few faulty panels and were not considered in the calculation of the RMS error. Progression to the final surface RMS included holography system checkout, so does not represent the time required to set the VertexRSI antenna to its final surface.

specification.

The best surface maps were obtained at night. During the spring 2003 period they consistently show an RMS of about 20 μm. Daytime maps tend to be somewhat worse; typical values of the RMS lie between 20 and 25 μm. Part of this is certainly due to the atmosphere, even over the short path length of 315 m.

AEC Antenna: The apex structure of the AEC antenna does not enable us to mount the holography receiver inside the apex structure cylinder, as in the case for the VertexRSI antenna. Thus in this case the receiver was bolted to the flange on the *outside* of the apex structure. Consequently, the feedhorn was brought to the required position by a piece of waveguide of about 500 mm length. This caused significant attenuation in the received signal from the reflector to the mixer. Considering the available transmitter power, we concluded that this would not jeopardise our measurement accuracy significantly.

The AEC antenna surface was set by the contractor with the aid of a Leica laser-tracker. The RMS of the surface was reported by the contractor to be 38 μm. After this measurement an accident caused the elevation structure to run onto the hard stops at high speed. The contractor decided to repeat the surface measurement and obtained an RMS of 50 μm with some visible "astigmatism" in the surface.

Our first holography map indicated an RMS of 55 μm with a clearly visible astigmatism. We could identify the high and low regions with those on the final AEC measurement. With two complete adjustments we surpassed the goal of 20 μm. A third partial adjustment improved the surface RMS to about 14 μm . There is no indication of the "artefact" seen in the VertexRSI antenna. There is one panel with a large deviation over part of the area. This is believed to have been caused during the measurement and setting procedure by the contractor. We have not included this panel in the computation of the final RMS value. The results of the consecutive adjustments are summarised in Figure 6. The last panel in this figure shows the final map after the repeated measurement and setting in January 2005.

The adjustments were done with a tool provided by the contractor. It was similar to the one used by us on the VertexRSI antenna, but it was calibrated in "turns" rather than in micrometres. Again two people on a manlift approached the surface from the front, where the adjustment screws are located. The time needed for an adjustment of the total of 600 adjusters was 7 hours, well within the specification of 8 hours.

Fig. 5.— Panel adjustment of the VertexRSI prototype antenna.

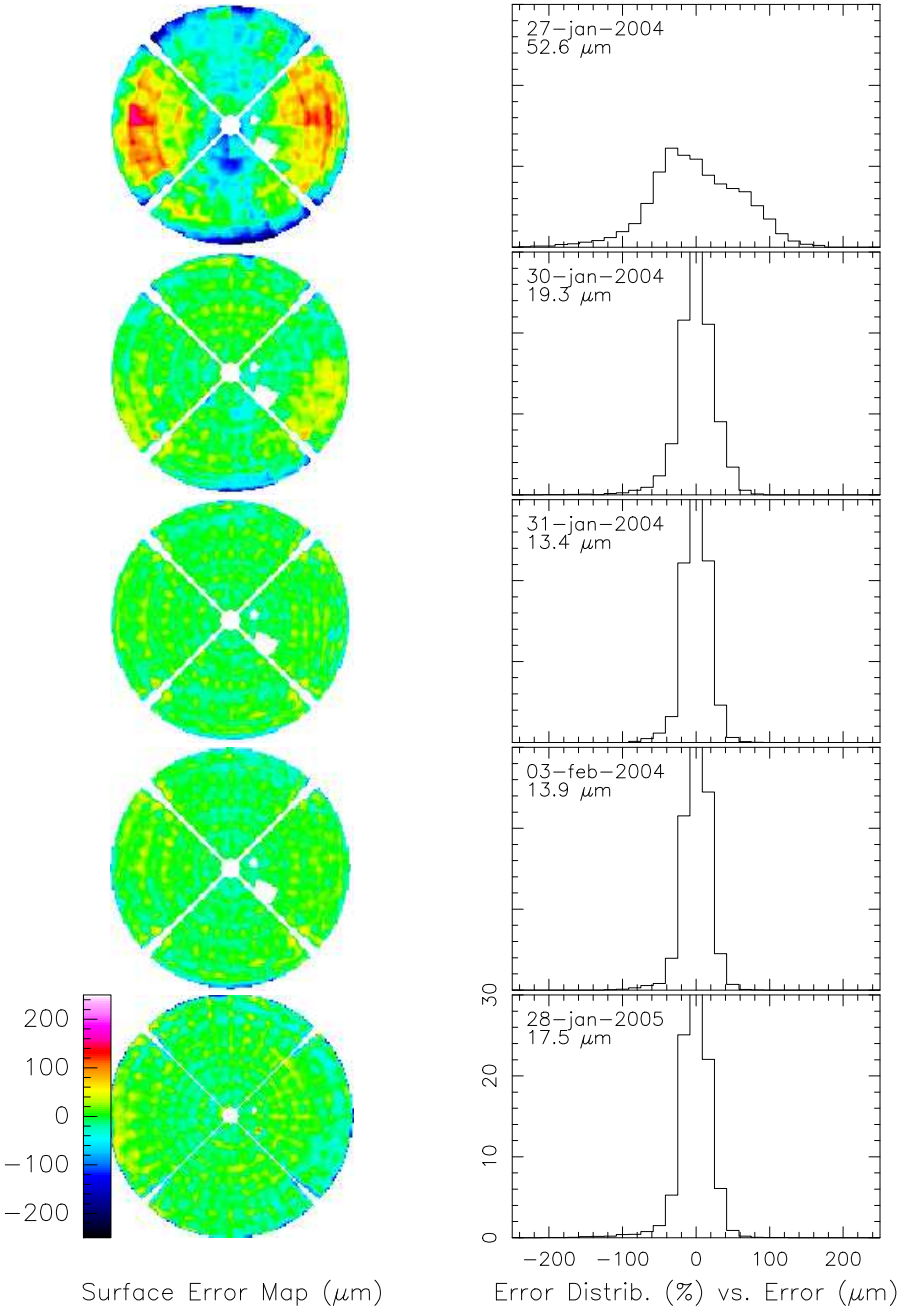

Fig. 6.— Sequence of surface error maps with intermediate panel setting for the AEC antenna. The surface contours are shown on the left side; the error distribution on the right. The white cross and the small white area represent the quadripod and a faulty panel and were not considered in the calculation of the RMS error.

5.1.2. Temporal Surface Stability

VertexRSI Antenna: To estimate the accuracy and repeatability of the measurements, we produced difference maps between successive measurements throughout the measurement period. The RMS difference between consecutive maps is typically less than 10 μm, and usually $\sim$ 8 μm. An example of a difference map is shown in Figure 7. The map of measurement number 307 is shown on the left, while the right hand side shows the difference between map 307 and 308, made about one hour later.

We have made many maps after the final setting of the surface while changing the orientation of the antenna with respect to the Sun. Maps taken over a few consecutive days were obtained at widely different temperatures, while also the wind conditions varied over time. The measured RMS error during a 30 hour period in early May 2003 varied between 20 and 23 μm. During this period the wind was calm ($<$ 5 m/s) and temperature changes of 15 C were encountered. A later 5 day series in mid June gave RMS errors from 22-26 μm with temperature variation up to 20 C, wind speeds up to 10 m/s and periods of full sunshine. Most of this increase is believed to be due to the deteriorating atmospheric conditions at the VLA site during summer, when the humidity was significantly higher than normal. The much better results of 17 μm obtained during the cold and dry winter period also point to a significant atmospheric component in the spring and summer results.

However, some of the changes will be caused by temperature and wind. To increase the RMS from 20 to 22 μm, the "additional" component has a magnitude of 9 μm RMS. Such a contribution can be expected from the calculated values of 4 μm each for wind and temperature for the panels, and 5 μm for wind and 7 μm for temperature for the BUS. These numbers are all within the specification. Actually, the measured differences are close to those expected from the estimated accuracy of the holography measurement and the measured RMS differences in consecutive maps of about 8 μm.

AEC Antenna: In Figure 8 we show one of the final results and a difference map of this and the following measurement, made one hour later. The difference map indicates a repeatability of $\sim 5\mu$m RMS. There is no indication of the wavy structure in the outer region of the aperture, as was the case for the VertexRSI antenna. We ascribe this to the lower signal level due to the long piece of waveguide between feed and mixer.

We made a series of 16 maps over a period of more than two days in early February 2004. Temperatures ranged from +2 to $-$10 C, while the wind was mostly calm with some periods of speeds up to 10 m/s. During one day there was full sunshine. The measured RMS error is very constant with a peak to peak variation of less than 2 μm on an average of 14 μm.

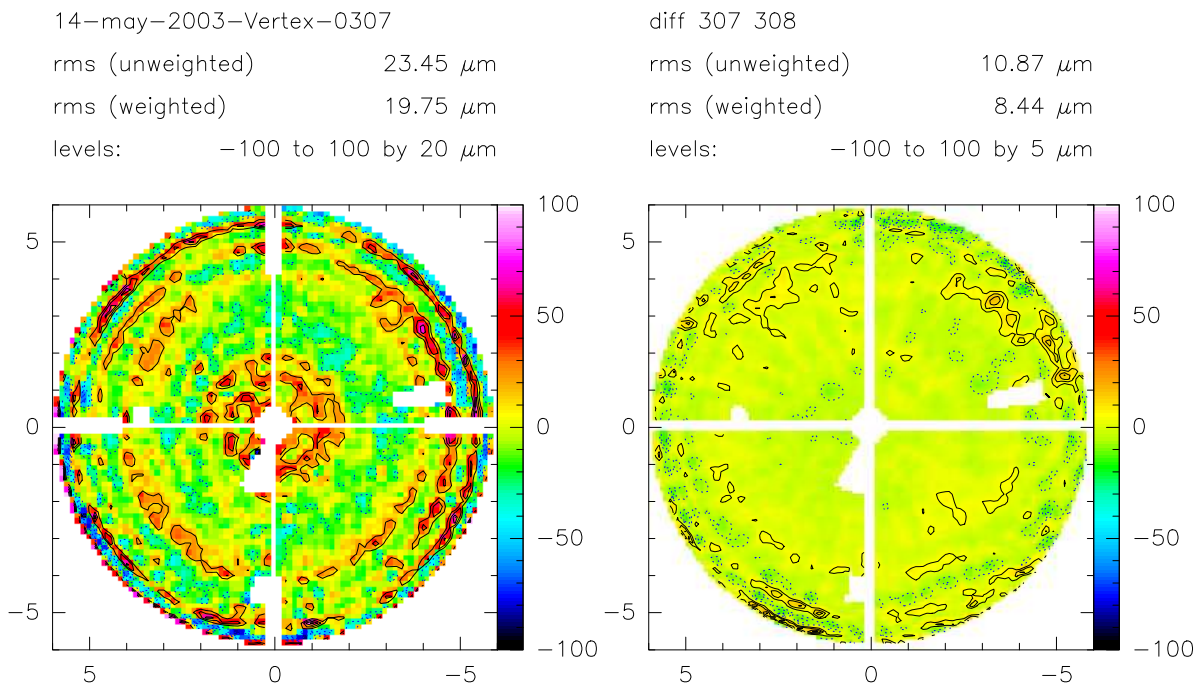

Fig. 7.— Example of the repeatability of the VertexRSI holography measurements. The map on the right is the difference between the one at left and a map made one hour afterwards. The RMS of the difference maps is about 8 μm, which is commensurate with the expected value due to noise and atmospheric fluctuations.

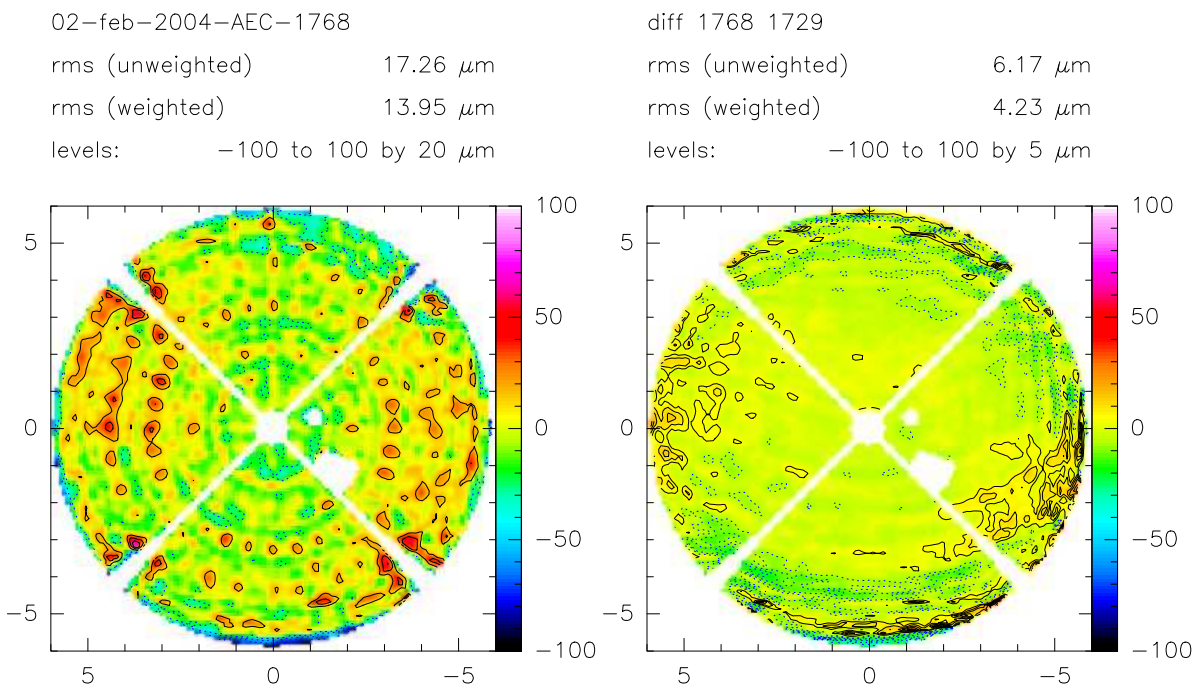

Fig. 8.— Example of the repeatability of the AEC holography measurements. The map on the right is the difference between the one at left and a map made one hour afterwards. The RMS of the difference maps is about 5 μm.

The differences are fully consistent with the allowed errors under environmental changes and also of the same order as the measurement accuracy. We believe that the significantly better overall result is mainly due to the much drier and more stable atmosphere during these measurements as compared with the summer data from the VertexRSI antenna.

5.1.3. Surface Stability with Changes in Ambient Temperature

VertexRSI Antenna: Further analysis of the VertexRSI time series data presented in §5.1.2 has been made to extract the dependence of the antenna surface to changes in ambient temperature. The analysis entailed the following:

- For each series the average of all maps in the series was subtracted from all the maps in the series. This suppresses dependencies on any long term effect.
- In each series the maps were divided into several temperature ranges; in each temperature range the average map was computed.
- Finally the difference between the coldest and warmest range averages were computed for each series. From these data we derived the surface deformation caused by a temperature change of 10 C, as shown in Figure 9.

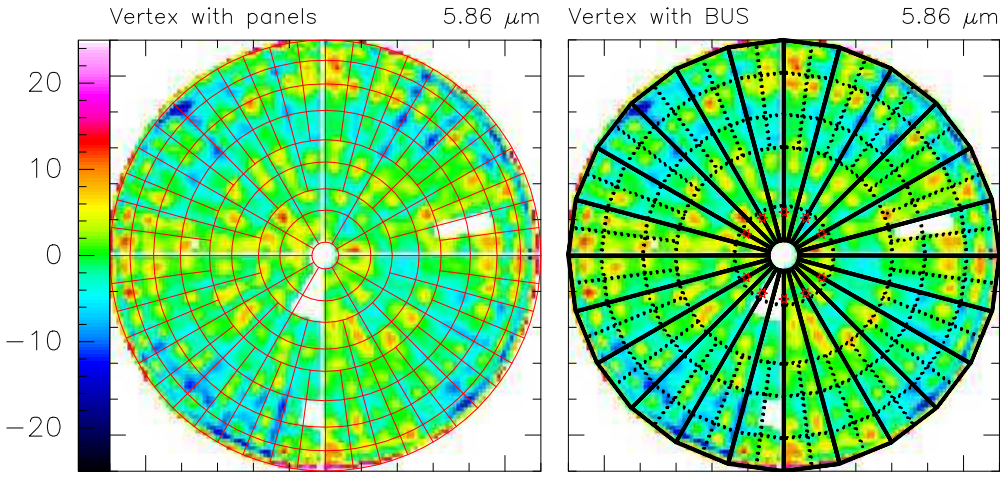

Fig. 9.— VertexRSI temperature span plots with panels (left) and BUS (right) boundaries overlain. To put these measurements on the same scale the data have been uniformly scaled to a temperature difference of 10 C. The RMS surface deformation over this 10 C temperature difference is indicated in the upper right.

From this analysis we note that:

- Many of the samples were for temperatures outside the primary operating range of -20 to $+20$ C.

- The results for the spring 2003 and winter 2005 periods are very consistent with each other.

- The magnitude of the RMS deformations is $\sim$ 0.6-0.7μm/K. This value seems high. It is not clear to which degree it should be split into panels and BUS and between absolute and gradient terms in the surface error budget. Assuming all effects to be linear with temperature, and antennas set at 0 C, we would expect RMS temperature contributions of $\sim 13\mu$m for the VertexRSI antenna at either end of the operational temperature range ($+20$ C or -20 C).

- The thermal deformations for the VertexRSI antenna appear to be a mixture of BUS (the BUS sector edge is sticking out at higher temperature) and panels, not all panels deforming equally.

- From the BUS overlay drawing (Figure 9) it appears that there is a print-through of the connections of the BUS with the Invar cone (the turnbuckles). The small red islands on (or just outside) the second stippled ring are at the diameter of the outer support of the BUS on the cone. We are not certain whether they are at or in between the connections to the cone. In both cases such a print-through might reasonably be expected.

- The BUS is also supported on the cone towards the center outside the inner stippled circle by about one fifth of the distance between the two stippled circles. Also there we see clear red islands of print-through. These effects are less pronounced in the "lower" section of the dish; actually they seem most pronounced in the left and right quadrants. We don't understand why this would be the case.

- There are clear, narrow "valleys" along the radials where the sectors of the BUS are joined, especially in the outer half of the radius. They are not equally strong all around, but visible in most cases. The inner part is less clear, presumably because of the already existing effects of the support points.

- From the map with the panel outline, and ignoring the islands connected to the BUS, as argued above, there is some but not very much evidence for individual panel deformations. It is most likely the case that individual panel deviations are caused more by forces originating in the stiffer BUS than from the panel itself.

AEC Antenna: Further analysis of the AEC time series data presented in §5.1.2 has been made to extract the dependence of the antenna surface to changes in ambient temperature. The analysis entailed the same sequence of calculation as those presented for the VertexRSI antenna (see §5.1.3). Figure 10 shows the temperature span assuming a uniform 10 C temperature difference.

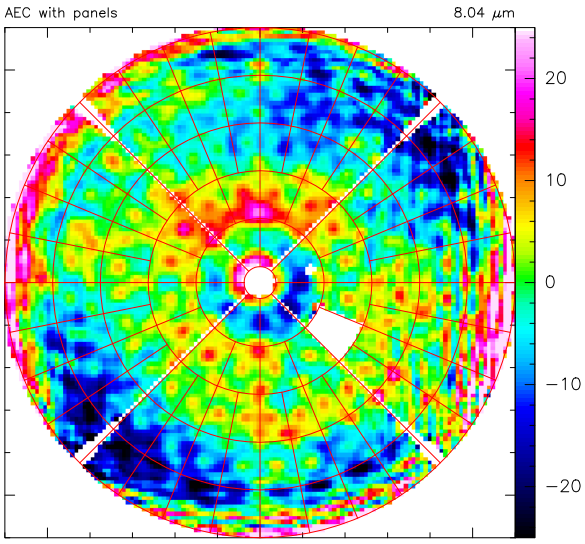

Fig. 10.— AEC temperature span plot with panel boundaries overlain. The data have been uniformly scaled to a temperature difference of 10 C. The RMS surface deformation over this 10 C temperature difference is indicated in the upper right.

From this analysis we note that:

- The sampled temperature range is completely inside the primary operating condition ambient temperature range of −20 to +20 C.
- The magnitude of the RMS deformations is $\sim 0.8\mu$m/K. This value seems high. It is not clear to which degree it should be split into panels and BUS and between absolute and gradient terms in the surface error budget. Assuming all effects linear with temperature, and antennas set at 0 C, we would expect RMS temperature contributions of $\sim 16\mu$m for the AEC antenna at either end of the operational temperature range (+20 C or −20 C).
- The large-scale deformation at 45 degrees position angle (which looks like astigmatism), along with the additional deformation of the inner ring, are hard to explain. These deformations are perhaps due to the temperature gradients in the cabin and the BUS,

coupled to the quadripod connection points. The vertical stripes on the edges of the AEC maps are an artefact of the measurement not related to temperature.

- In principle there should be little print-through structure in the difference maps, due to the fact that the BUS design is more homogeneous, being all CFRP, and it should have a continuous transfer of forces to the cabin, which is also the same material.
- We don't see any individual panel deformation.

5.2. Near-Field Holography Measurement Conclusions

1. The holography system has functioned according to specification and has enabled us to measure the surface of the antenna reflector with a repeatability of better than 10 μm.
2. As shown in Figures 4 and 6, we have set both antenna surfaces to an accuracy of 16-17 μm RMS. This will provide an aperture efficiency of about 65 percent of that of a perfect reflector at the highest observing frequency of 950 GHz.
3. The small differences in the surface maps obtained over several days of measurement are consistent with the measurement repeatability and at best marginally significant. If taken at face value, they indicate that the deformations of the reflector under varying wind and temperature influence are fully consistent with, and probably well within, the specification. This excellent behaviour over time is more important than the actual achieved surface setting. We stopped iteration of the settings after having achieved the goal of less than 20 μm.
4. The measured variations with ambient temperature changes appear somewhat large. They correspond to a thermal contribution to the surface error of 10–16 μm at the boundaries of the operational range (-20 and $+20$ C), assuming a setting at 0 C. This is slightly more than the contribution in the "ALMA error budget" and also more than the prototype antenna contractors have budgeted. On the other hand, taking BUS, panel and adjuster error contributions all together leads to approximate agreement with these measurements.
5. Within the primary operating range for ambient temperature of -20 to $+20$ C the surface error budget of the production antennas allows for a BUS contribution of 8 μm due to absolute temperature change and 7 μm for gradients. The panels are allowed 4 μm for absolute temperature and temperature gradient each. If we assume that the surface is set at 0 C to a measured value of 15 μm, which is the value we achieved,

and we add the 15 μm maximum of the temperature deformation, the resulting error is 22 μm. This is more than the goal, but well within the specification. High mountain sites, including Chajnantor, generally experience wind. This will dampen temperature gradients in the antenna structure and hence decrease the resulting structural deformation.

5.3. Accelerometer Measurements of BUS Deflection

Accelerometers are used to measure accelerations in the inertial coordinate system of the antenna, allowing determination of rigid body motion of the elevation structure, and a few low-order distortions of the BUS. In addition, motion of the subreflector structure with respect to the BUS can be measured. For the BUS deformation measurements 10 accelerometers were placed on the BUS in the following configuration (Figure 11):

- 3 accelerometers as a 3-axis sensor on the subreflector structure (numbered 1, 2, and 3 in Figure 11)
- 4 accelerometers along the rim of the BUS in boresight direction (numbered 4, 5, 6, and 7 in Figure 11)
- 3 accelerometers as a 3-axis sensor on the receiver flange Invar ring (numbered 8, 9, and 10 in Figure 11)

The nature of the accelerometers used here limits accurate displacement measurement to timescales of at most 10 seconds or frequencies of at least 0.1 Hz. Since this is well below the lowest eigenfrequencies of the antennas, this is sufficient to determine dynamic antenna behaviour. See Snel et al. (2006) for further information about the ALMA accelerometer measurement system.

Over the 0.1 to 30 Hz sensitivity range of the accelerometers, the changes in reflector surface shape through measurements of the focal length (Zernike polynomial Z3 "power", "defocus" term, n=2, m=0) and "+" astigmatism (Zernike polynomial with n=2, m=2) can be measured to better than a few micrometers.

5.4. BUS Deflection Measurement Conclusions

For 9 m/s wind over time scales of 15 minutes, the VertexRSI antenna surface is stable to 5.3 μm astigmatism RMS at the rim of the BUS, and 2.2 μm defocus. The AEC antenna

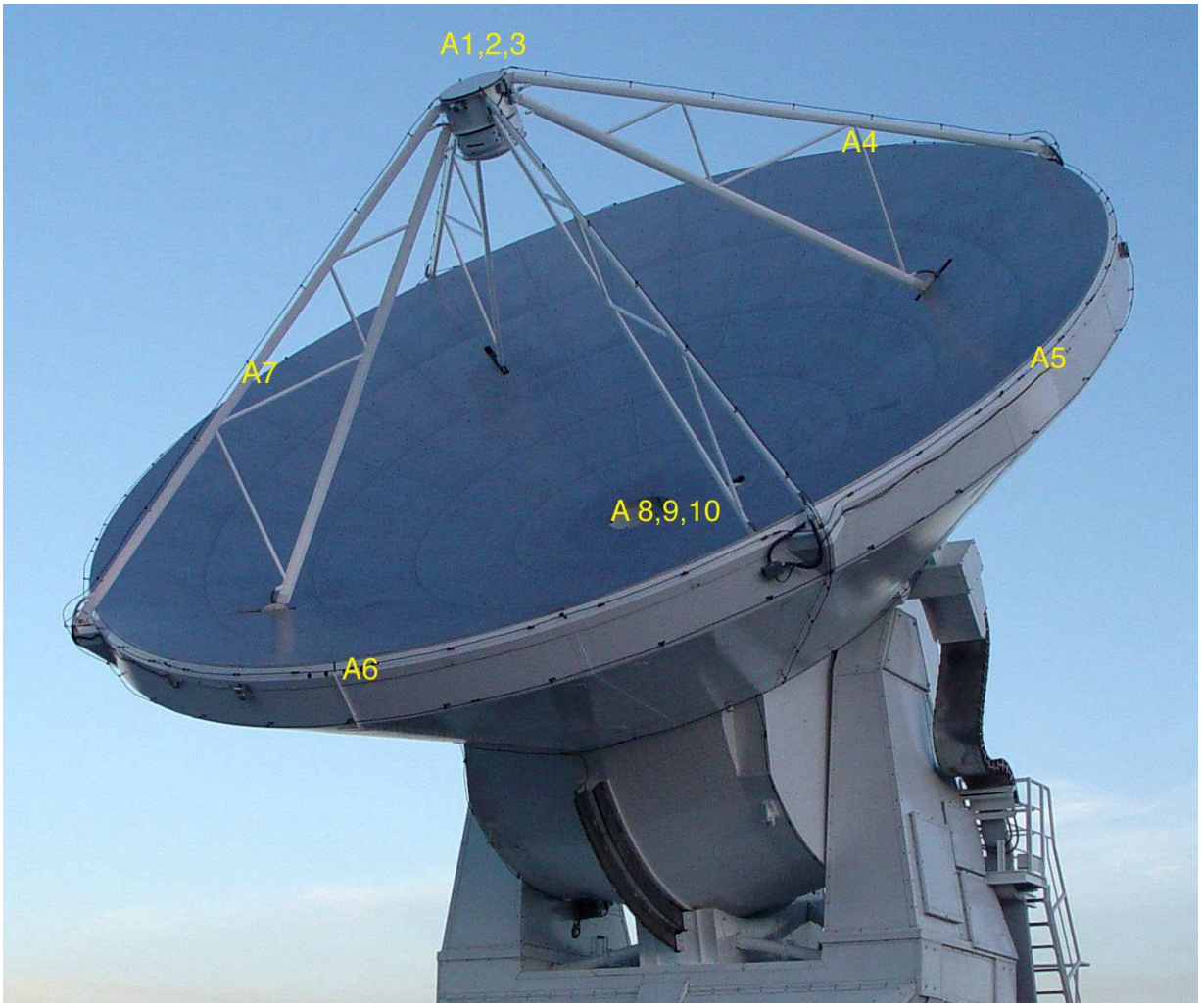

Fig. 11.— Placement of the accelerometers on the antenna for BUS deflection (surface accuracy) measurement.

surface is stable to 6 μm astigmatism RMS at the rim of the BUS, and 5 μm defocus. For both antennas, surface stability is dominated by the stiffness of the BUS for wind excitation at low frequencies. The measured values are in reasonable agreement with the error budget numbers from the contractors. Note that these values do not include gravitational and thermal effects. During sidereal tracking the astigmatism and defocus deformations remain below 1 μm for both antennas.

A frequently used operational mode of ALMA is "fast switching", in which the antennas are pointed alternately at the observed source and a nearby calibration source 1-2 degrees away typically at 10 second time intervals. The antennas are designed to achieve such a switch

within 1.5 seconds. It is of interest to measure the dynamical behaviour of the antenna structure during such switching cycles. During the strongly accelerated and decelerated movement we measure negligible BUS rim deformations of the order of one millimeter, which decrease to a few micrometers after the new position has been reached.

During "On-The-Fly" (OTF) observing, the antenna scans a region of sky back and forth at 0.5 deg/sec speed. During this movement we measure astigmatism at the reflector edge and a defocus movement of a few micrometers each. Interferometric mosaicing at 0.05 deg/sec causes barely measurable astigmatism and defocus stability of about 1 μm.

Within the sensitivity of these measurements it can be stated that both antennas exhibit dynamical deformations of the reflector surface that are small and in agreement with the surface error budget. Also, as these measurements demonstrate, very small dynamical deformations can reliably be measured with this accelerometer setup. We consider this method, pioneered by Ukita & Ikeda (2002) and also used on an optical telescope by Smith et al. (2004), of great potential for the study of the dynamical behaviour of large and highly accurate telescopes.

6. Absolute and Offset Pointing

In the following we describe the analysis of the pointing performance of the two ALMA prototype antennas. The analysis is (mostly) based on optical pointing observations carried out between October 2003 and May 2004 and radio pointing measurements carried out during March 2004 (VertexRSI) and May 2004 (AEC). The optical and radio pointing data analysis was carried out using the proprietary TPOINT telescope pointing-analysis software. The AEC results are more limited than those from the VertexRSI antenna and cover a shorter time span, because of late handover of that antenna.

This pointing analysis studies three aspects of the antennas:

1. All-sky blind pointing accuracy. In the optical case:
   - Find the model that best describes the all-sky pointing for the antenna under study, in its "optical pointing test configuration".
   - Find the best coefficient values for use in the 7-term ALMA "standard internal model" (§6.1.2).
   - Estimate the best all-sky optical pointing performance that could be expected operationally (§6.3).

- Assess the stability of the optical pointing model (§6.3.4).

In the radio case:

- Find the model that best describes the all-sky pointing for the antenna in question when operating in its radio configuration (in particular at 95 GHz).
- Estimate the best all-sky pointing performance that could be expected operationally.

2. Assess the smoothness of tracking (optical, and for one antenna only).

3. Determine the ability to offset accurately across short distances (optical only).

In all, the pointing analysis of the ALMA prototype antennas relied on measurements made with three distinct systems:

- An optical pointing telescope (OPT) mounted within the BUS of each antenna. The OPT is a NRAO-designed refracting telescope composed of a 4 inch lens mounted within a rolled-Invar tube (Mangum (2004)). The detector used was a commercial CCD camera coupled to a video frame grabber. Figure 12 shows two typical absolute (all-sky) pointing residual plots obtained with the OPT system.
- Radiometric measurements at 1 and 3 mm wavelength. Figure 13 shows a sample single dish image obtained with this receiver system.
- An accelerometer system (§6.8).

Both prototype antennas were designed to meet the pointing specifications with the aid of various metrological correction systems. These metrology systems were in general unsuccessful at improving the pointing performance of the prototype antennas, as described in §6.6.

6.1. Pointing Models

6.1.1. TPOINT Modeling

If a telescope or antenna is pointed at a star, there is in general a difference between the true direction of the incoming light and the demands to the mount servos, due to mechanical

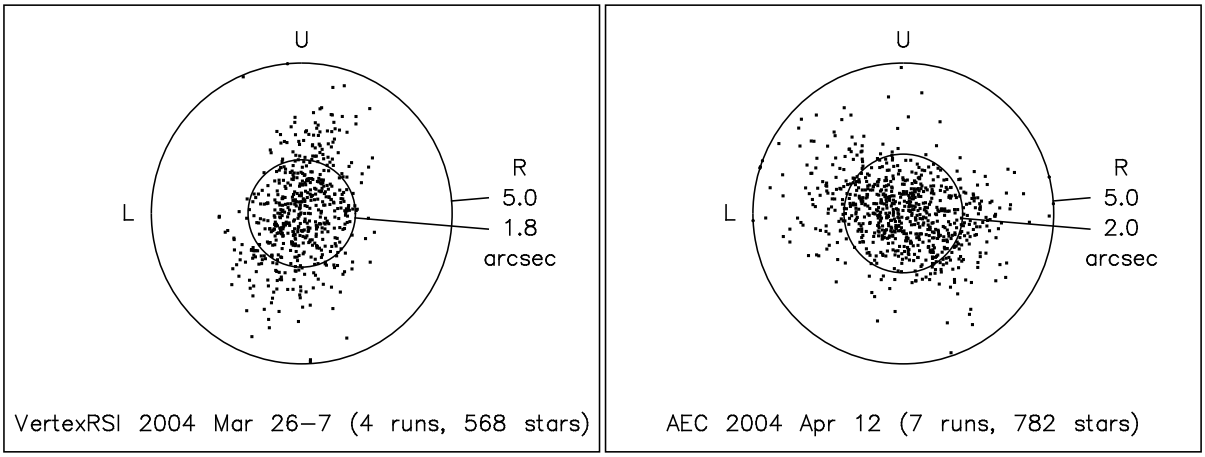

Fig. 12.— Left: Sample VertexRSI (left) and AEC (right) OPT pointing residual plots. Shown are the measurement residuals following application of the respective pointing models, each comprising 13 terms. The outer ring marks a radial residual of 5 arcsec, while the inner ring indicates the RMS pointing residual for each antenna.

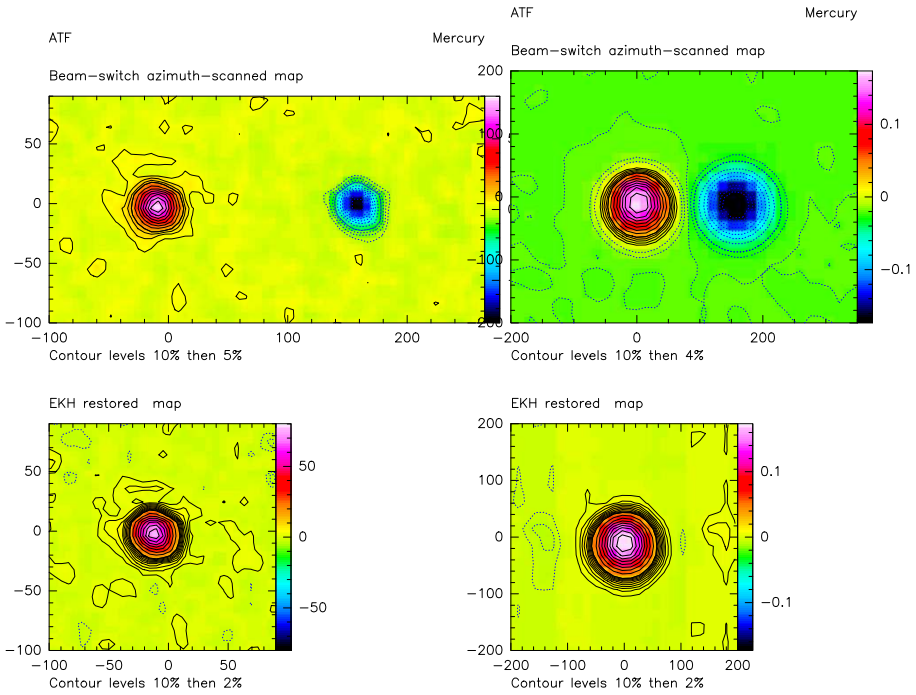

Fig. 13.— Beam-switched radiometric measurements of the planet Mercury. Left: VertexRSI measurement made at 265 GHz. Mercury was at an angular distance of 16 degrees from the Sun, the planet angular diameter was 5.1 arcsec, and the contour levels are 5,10,20, ..., 90 %. Top: raw beam-switched map (beam separation 160 arcsec); bottom: map restored using the EKH (Emerson et al. (1979)) algorithm; contour levels are 2, 4, ..., 16, 18, 20, 30, ..., 90%. The low-level structure located $\sim$ 35 arcsec seen in both restored and unrestored maps is due to a slight defocus in the Y-coordinate. Right: AEC measurement made at 95 GHz. Mercury was at an angular distance of 25 degrees from the Sun, the planet angular diameter was 7.2″, and contour levels are $4, 8, 12, 16, 20, 30, ...$90%. Top: raw beam-switched map (beam separation 160″); bottom: map restored with the EKH algorithm; contour levels are $2, 4, 8, ..., 16, 18, 20, 30, ...$90%.

misalignments, flexures and other imperfections. By observing stars all over the sky and logging the actual and commanded positions (or data from which these angles can be deduced), a mathematical model can be developed that estimates the servo inputs required to point the antenna accurately in a given direction. The TPOINT pointing analysis software reads a file containing the logged observations and provides graphics and modeling tools that allow a mathematical description of the pointing errors to be created. The resulting pointing model has then to be built into the telescope or antenna control system, so that the demands to the servos are appropriately adjusted and accurate dead-reckoning acquisition of celestial targets brought about.

For any two-axis "gimbal" mount, the basic *a priori* model consists of seven terms: two encoder index errors, two non-perpendicularities, two azimuth-axis tilt components, and Hooke's Law flexure. All of these terms have a clear mechanical interpretation and, in general, all will be present to some degree. This basic model usually performs well, typically leaving only a small remaining systematic residue to be mopped up using the repertoire of other TPOINT terms. Most of the latter set out to represent plausible mechanical effects—for example harmonic terms to deal with run-outs and mechanical deformation errors—though it is also possible to introduce unashamedly empirical terms such as polynomials should there be no alternative.

Table 3: The Seven Basic Pointing Model Terms

Term	Correction Formula		Nominal Cause
	ΔAz	ΔEl	
IA	$-$IA	...	Az encoder zero point offset
IE	...	+IE	El encoder zero point offset
HECE	...	$+\text{HECE}\cos E$	Hooke's Law vertical flexure
CA	$-\text{CA}\sec E$	...	Non-perpendicularity between the boresight and El axis
NPAE	$-\text{NPAE}\tan E$	...	Non-perpendicularity between the Az and El axes
AN	$-\text{AN}\tan E\sin A$	$-\text{AN}\cos A$	Az axis offset/misalignment north-south (north = positive)
AW	$-\text{AW}\tan E\cos A$	$+\text{AW}\sin A$	Az axis offset/misalignment east-west (west = positive)

The functional form of the basic 7-term model is given in Table 3. Note that:

- The sign of the correction terms is such that the expressions should be subtracted from the true direction in order to generate mount demands.

- The coefficient values in service will either be those from the most recent set of observations or averages of several recent runs.
- The expressions are approximate, adequate when the coefficients are small and/or the target is not too close to the zenith. TPOINT in fact fits rigorous vector formulations that do not have these limitations.

6.1.2. The Standard ALMA Internal Model

The *a priori* 7-term model (Table 3) is also that specified by ALMA for internal implementation in the low-level antenna controllers, principally as an aid to commissioning. Once the final TPOINT model is available, the optimum coefficients to be used with this basic 7-term model can be estimated by subtracting the full model from a set of points distributed evenly over the sky, then fitting the 7-term model. The final RMS from such an experiment represents the maximum achievable performance of the ALMA internal model for the antenna in question, while the residual plots illustrate the antenna's pointing idiosyncrasies. This experiment was carried out for both antennas, using OPT data, for illustrative purposes. For the AEC antenna, the best-fit sky RMS was 2.46 arcsec. For the VertexRSI antenna, the best-fit sky RMS was 3.25 arcsec. The limitations of this simple 7-parameter model are illustrated in Figure 14.

6.2. The ALMA Optical Pointing Telescopes

Optical pointing systems have become standard equipment on millimeter and submillimeter telescopes. There are benefits and limitations associated with the reliance on optical pointing systems on radio telescopes:

1. Benefits:
   (a) There are many more bright stars that can be used as optical pointing sources than radio pointing sources.
   (b) With a CCD camera, optical data acquisition can be done on time scales as short as a few tenths of a second, as opposed to the tens of seconds time scales necessary for radio pointing measurements.
   (c) Positions of optical stars can be derived to sub-arcsecond accuracy, which is a much higher precision than that obtainable through single antenna radio measurements.

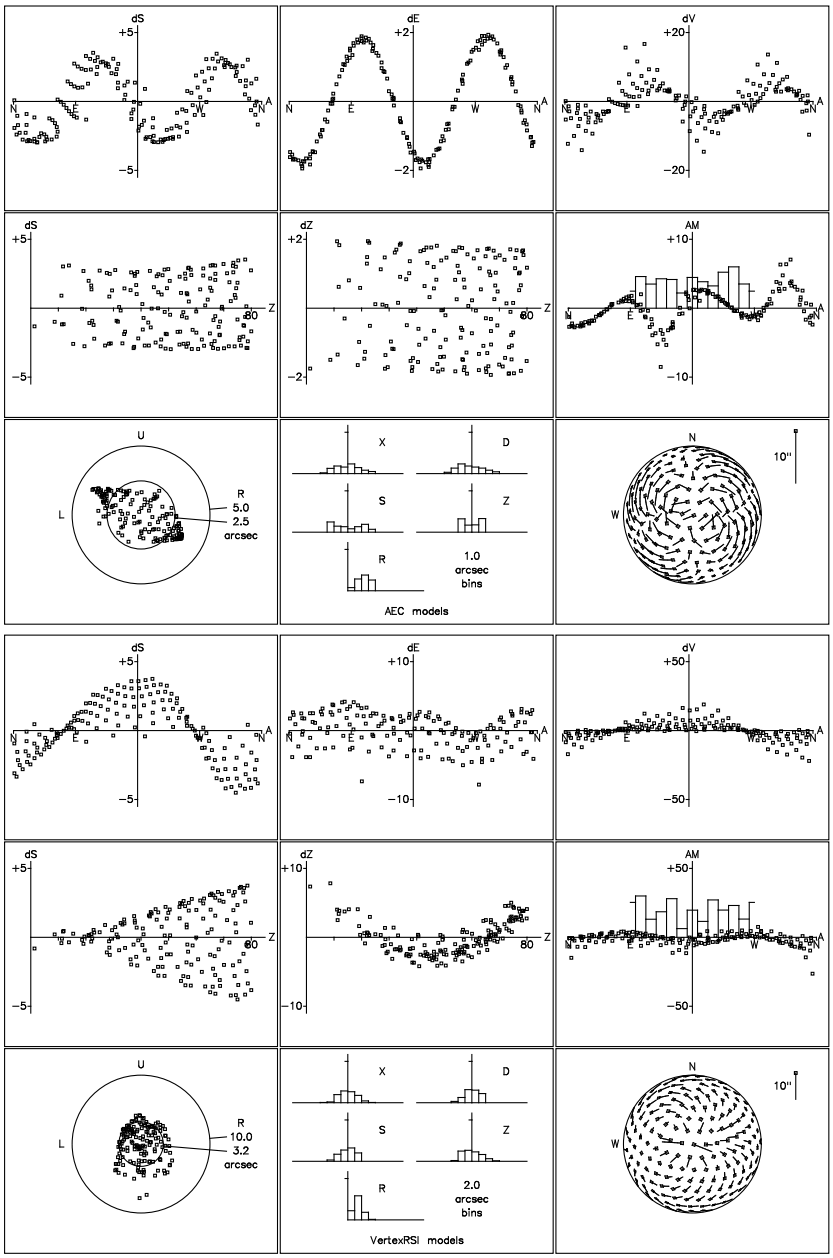

Fig. 14.— The predicted pointing model residuals using the AEC (top) and VertexRSI (bottom) 7-parameter pointing models. The panels show, left-to-right: (top row): $\Delta A \cos(E)$, ΔE, and inferred Az/El nonperpendicularity versus A; (middle row): $\Delta A \cos(E)$ and ΔZ (zenith angle) versus Z, and azimuth axis tilt versus A; (bottom row): pointing residual versus (A,E), pointing residual histogram versus all coordinates, and pointing residuals on an all-sky pointing error vector map. The limitations of these simple models are apparent.

2. Limitations:

   (a) Differences between the position and behavior of the optical and radio signal paths can make the derivation of the radio pointing coefficients from optical pointing measurements difficult.

   (b) Optical pointing is not possible during overcast weather conditions.

   (c) Optical pointing cannot be used in the daytime, unless the system has been designed with near-infrared sensitivity.

Optical pointing systems find application in such areas as:

- Pointing and tracking diagnosis
- Pointing coefficient derivation and monitoring
- Auto-guiding

Table 4 lists the ALMA prototype optical telescope system specifications (Mangum (2004)).

6.2.1. Optical Telescope Measurement System Limitations

1. The optical seeing at the VLA site is generally poor. To quantify this seeing contribution to the OPT measurements a sequential multiple star measurement, where each star measurement was repeated three times, was used to derive seeing and/or short timescale antenna positioning errors. These measurements suggest a seeing/vibration contribution of ∼1.5 arcsec, in line with the results from tracking tests. With the OPT's 100 mm aperture, the seeing manifests itself as large and rapid movements of the image, making optical measurement of the all-important tracking and offsetting performance almost impossible.

2. The OPT design, which was always going to be a major challenge, is itself marginal for this application, given the impressive performance of the antennas. The comparatively short focal length means that the image is under-sampled, and in some of the tracking tests quantization effects are evident, making performance limitations much below 1 arcsecond difficult to detect. It is far from obvious how to deal with this; a refracting OPT of (say) twice the aperture would have been prohibitively expensive, and also very large, whereas a reflector (a commercial Schmidt-Cassegrain for example) would probably have had insufficient optical stability.

Table 4: Prototype ALMA Optical Telescope Specifications

Telescope	Meade 4″ model 102ED Apochromatic Refractor
	f/9 (920mm focal length)
	NRAO-design rolled Invar tube and mount
Additional Lenses	X2 Barlow
Filters	IR continuum ($\lambda > 700$nm) and clear focus correction
Camera	Cohu 4920-3000 camera
	Extended IR sensitivity to 900nm
	56 dB dynamic range
	768×494 pixels
	8.4×9.8 μm pixel size
	6.4×4.8 mm image area
Frame Grabber	Imaging Technologies PC-Vision
	1024×1024 array capability
	640×480 sampling (RS-170)
	2MB VRAM
	4ms frame transfer
	48 dB dynamic range
Control PC	COTS
Control Software	NRAO design
Diffraction Limit	1.″2 (for $\lambda = 500$ nm)
Plate Scale	0.1121 arcsec/μm
Effective Plate Scale	$1.''12 \times 1.''12$ per detector pixel
Field of view	$12' \times 9'$
Sensitivity	$\geq 7^{th}$ magnitude in 5 second exposure
Mount location	Backup structure (requires access hole in panel)
Mount	Three-point Invar; accessible

6.3. Optical Pointing Telescope Measurements

6.3.1. Data Acquisition

The pointing measurement data logging procedure evolved during the antenna evaluation process, ultimately leading to a very self-consistent and robust scheme for position calculation and logging. We refer to this final position calculation and logging scheme as "PMDR" (Pointing Model Done Right).

The two schemes (pre-PMDR and PMDR) are illustrated in Figure 15. In the pre-PMDR mode the inputs to the TPOINT pointing analysis are (i) the "observed" azimuth

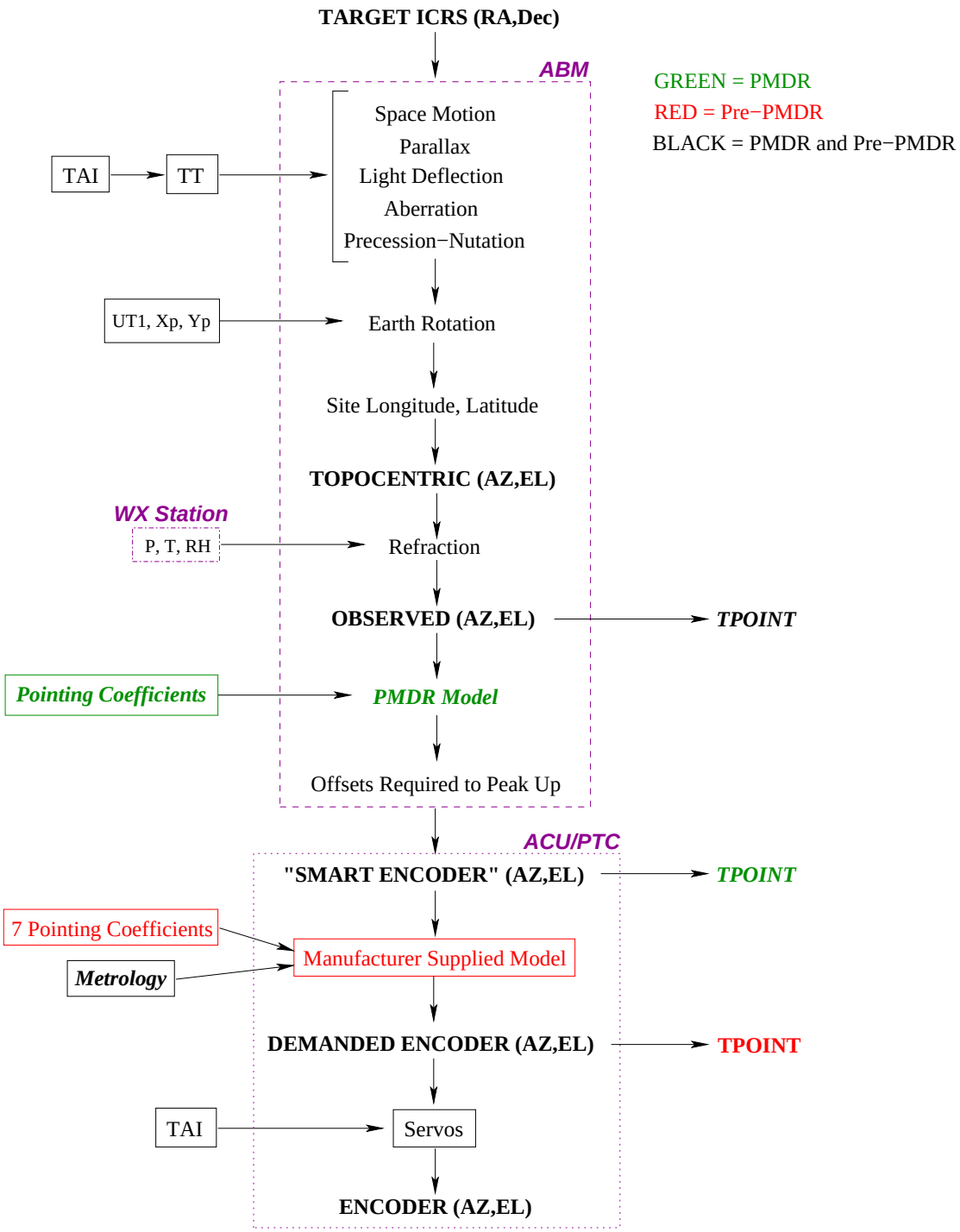

Fig. 15.— Positioning calculation flow for the pre-PMDR and PMDR systems. The roles of the respective computers are shown boxed.

and elevation (*i.e.* the true line of sight) and (ii) the encoder readings from the mount axes. The TPOINT analysis produces updated pointing coefficients for the ALMA internal 7-term model, calculated to minimize the offsets required to peak up on a new source and, equivalently, the drifts during subsequent tracking. Note, however, that coefficients obtained in this way presume zero metrology input; they are not suitable for use with metrology enabled, and the fitting statistics (*e.g.* RMS) do not reflect any benefits coming from the metrology system. Moreover, if use with the manufacturer's supplied control system is envisaged, the TPOINT model is limited to the seven standard terms (from Table 3), and additional forms of correction are not available. This final point proved to be a major handicap, hampering the pointing performance characterization of the ALMA prototype antennas and limiting the ultimate performance (see Figure 14).

These shortcomings were addressed by the PMDR scheme (see the green items in Figure 15). In this scheme, the quantities logged for input to TPOINT are (i) the observed (Az,El) as before but this time (ii) the commanded inputs to the manufacturer's model and metrology systems, the latter constituting a "smart encoders" interface. The link between the two is a separate TPOINT model that can contain any required terms, not just the seven basic terms. In fact it is advantageous to disengage the manufacturer's model, so that the TPOINT model provides the whole correction apart from the metrology inputs: the end result is the same and the TPOINT model then represents absolute physical estimates – nonperpendicularies, misalignments, flexures, *etc.* All measurements quoted in the following analysis used the PMDR positioning and logging scheme.

6.3.2. All-Sky Optical Pointing Data

The respective data samples for each prototype antenna are listed below. For both samples, we note that:

- The short time span available for evaluating pointing performance unfortunately precluded any studies of the long term stability of the pointing terms.
- A handful of these pointing tests were carried out with contractor-delivered metrology systems. We describe the results of these few metrology tests in §6.6.
- To obtain the total sample of measurements for both antennas, individual runs were for the most part accepted or rejected on the basis of notes made at the time they were carried out, rather than whether they gave better or worse pointing residuals. However, certain runs were clearly aberrant. These obviously untypical runs were rejected.

AEC: A selection of 63 pointing test runs were carried out during an intensive period of testing between 2004/03/06, when the antenna first became available, and 2004/05/12. There were a total of 7411 observations in this sample. Following some modifications by the antenna contractor in December 2004, an additional series of measurements were made during the period 2005/01/07 and 2005/03/02. As these additional measurements are not directly comparable to those made during the 2004/03/06 through 2004/05/12 period considered here, we defer their analysis to §6.3.5.

VertexRSI: A selection of 34 pointing test runs that utilized the PMDR positioning system (see §6.3.1) were carried out between 2004/03/10 and 2004/05/03, comprising 4059 observations.

6.3.3. The OPT Core Terms

In the final optical pointing derived models we have distinguished the set of floating basic pointing terms—IA, IE, CA, AN, AW—from a fixed "core" set of terms that are not only considered to have a specific mechanical cause but can also be assumed to be fixed in size. Moreover, for most of these core terms there is no reason to suppose that they will be affected by the transition from optical to radio pointing.

The core terms for both prototype antennas are listed in Table 5. For each term we list the nominal mechanical deformation that produces each term. Note that:

- The sign of the correction terms is such that the expressions should be subtracted from the true direction in order to generate mount demands.
- The smallest terms are of order 1 and 0.5 arcsec in size for the AEC and VertexRSI models, respectively. Their significance can be gauged by eliminating the smallest of them, namely HESA2 (AEC) and HECA3 (VertexRSI), fitting the full model to take up the slack, and plotting the residuals. The result of this experiment shows a distinct $\sin(2A)$ (AEC) and $\cos(3A)$ (VertexRSI) systematic residual in ΔEl versus Az for the respective antennas. Figure 16 shows the graphical results for the AEC antenna.

6.3.4. Stability of the OPT Pointing Model

In principle, all of the terms of an antenna's pointing model should maintain constant amplitude for long periods unless something on the antenna has been adjusted. This sup-

Table 5: OPT Core Pointing Model Terms

Term	Ampl. (VertexRSI/AEC)	Correction Formula	Nominal Cause
HESE	NA/−27.56	$\Delta E = +\mathrm{HESE}\sin E$	El encoder run-out, sine component
HECE	+30.09/−16.85	$\Delta E = +\mathrm{HECE}\cos E$	El encoder run-out, cosine component and/or vertical flexure
HASA	−1.20/NA	$\Delta A = +\mathrm{HASA}\sin A$	Az encoder run-out, sine component
HACA	−4.42/NA	$\Delta A = -\mathrm{HACA}\cos A$	Az encoder run-out, cosine component
HASA2	+0.73/−1.70	$\Delta A = +\mathrm{HASA2}\sin 2A$	Az encoder tilt, sine component
HACA2	NA/+2.94	$\Delta A = -\mathrm{HACA2}\cos 2A$	Az encoder tilt, cosine component
HESA2	NA/−0.99	$\Delta E = +\mathrm{HESA2}\sin 2A$	El nod twice per Az rev, sine component
HECA2	NA/+1.53	$\Delta E = +\mathrm{HECA2}\cos 2A$	El nod twice per Az rev, cosine component
HASA3	+0.38/NA	$\Delta A = +\mathrm{HASA3}\sin 3A$	Az encoder error 3× per rev, sine component
HESA3	+0.94/NA	$\Delta E = +\mathrm{HESA3}\sin 3A$	El nod 3× per Az rev, sine component
HECA3	−0.34/NA	$\Delta E = +\mathrm{HESA3}\cos 3A$	El nod 3× per Az rev, cosine component
HVSA2	NA/−2.25	$\Delta A = +\mathrm{HVSA2}\sin 2A\tan E$	Az/El nonperp variation twice per Az rev, sine component
HVCA2	NA/−2.08	$\Delta A = -\mathrm{HVCA2}\cos 2A\tan E$	Az/El nonperp variation twice per Az rev, cosine component
NPAE	−15.01/+28.62	$\Delta A = +\mathrm{NPAE}\tan E$	Az/El non-perpendicularity

position was studied by taking the individual models for the series of pointing tests on each antenna, and plotting the coefficient values for the five terms thought most likely to be affected by mechanical adjustments and drifts. The stability of these coefficient values were then studied by plotting them versus sequence number (in effect versus time).

For the AEC antenna, the stability of the five basic pointing model terms over the period 2004/03/06 through 2004/05/12 was (ΔIA, ΔIE, ΔCA, ΔAN, ΔAW) = (±3, ±5, ±3, ±1, ±1) arcsec, with very little drift of the average values for each term. This is very good basic pointing term stability for an antenna. The VertexRSI antenna pointing term stability over a much longer measurement period (2003/10/16 to 2004/03/01) was (ΔIA, ΔIE, ΔCA, ΔAN, ΔAW) = (±3, ±7, ±5, ±5, ±3) arcsec, with very little drift of the average values for most terms (the AN term showed a moderate ~ 5 arcsec drift of the average during the measurement period). The basic pointing model term stability for the VertexRSI antenna was notably worse than that of the AEC antenna. Part of this poorer performance is likely attributed to the failure of the tiltmeter metrology system (see §6.6), which was designed to correct for variations in the azimuth axis tilt (AN and AW).

6.3.5. Additional OPT Measurements of the AEC Antenna

Following the all-sky OPT measurements described above the antenna contractor made some modifications designed to improve the all-sky pointing performance. In particular, the attachment points of the antenna base to its foundation were tightened, and a tiltmeter-based metrology correction was enabled in an attempt to correct the suspected instability in the azimuth bearing. An additional series of measurements were made during the period 2005/01/07 and 2005/03/02 following these modifications. From these measurements we note that:

- Two terms – HVSA2 and HVCA2 – were no longer significant and need not exist in the pointing model solution. The HVSA2 and HVCA2 terms represent changes in the Az/El nonperpendicularity as the mount rotates. The insignificance of these terms suggests that the Az axis had become less wobbly.

- Figure 17 shows the cumulative AEC optical pointing model results for this period. For each total RMS value shown we also show the contributions to this total RMS due to cross-elevation and elevation pointing residual.

- A large observed shift in the IA and AW pointing terms, relative to the previously-derived pointing models reported in Wallace et al. (2004), was ultimately diagnosed as

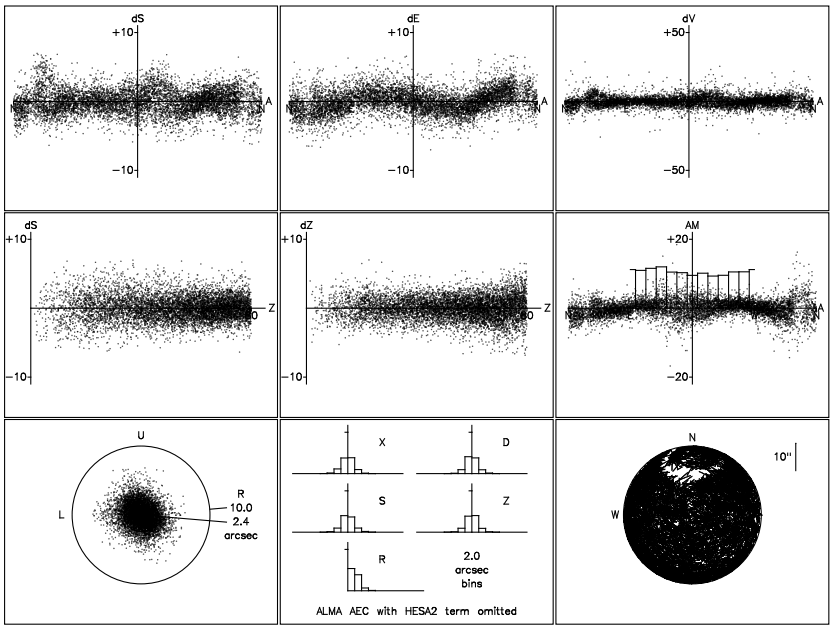

Fig. 16.— TPOINT plot showing the significance of the HESA2 term for the AEC antenna pointing model. Note the clearly systematic residual in ΔEl versus Az in the top-middle panel, suggesting the need for a $\sin(2A)$-dependent term.

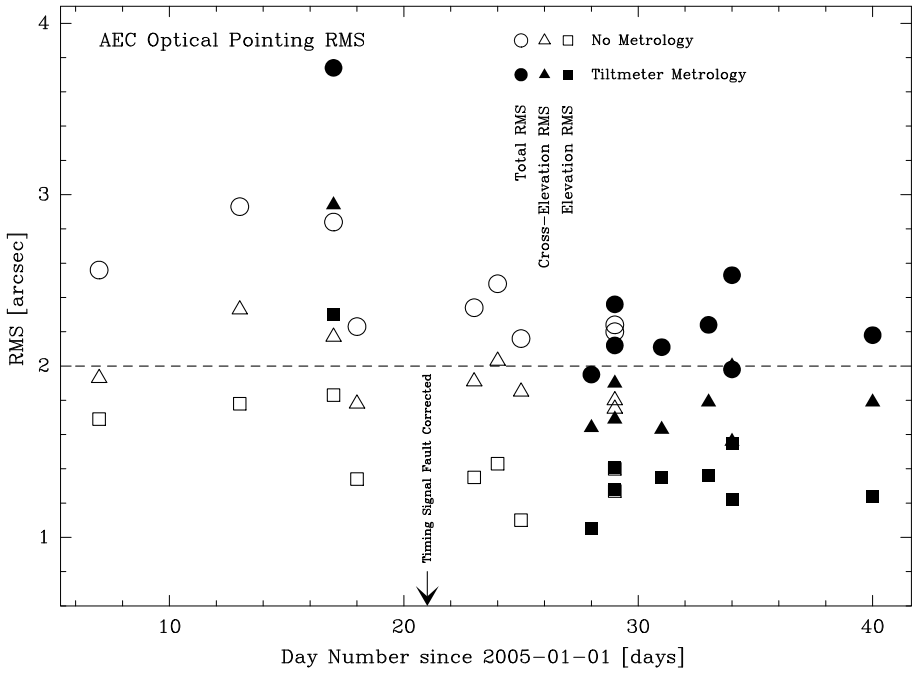

Fig. 17.— AEC optical pointing results for the period 2005/01/07 – 2005/03/02.

a timing error in the monitor and control system of approximately 13 seconds. This timing error does not affect the resultant pointing RMS values derived. On 2005/01/20 this timing error was corrected.

- A timing signal cable problem was fixed on 2005/01/23.

6.3.6. Pointing Model Recalibration Frequency

The ALMA pointing specification permits monthly recalibration of the pointing model. To investigate this, two representative all-sky OPT runs taken a month apart were chosen. The first was used to simulate the periodic recalibration of the five "non-core" terms of the AEC model (IA IE CA AN AW). This simulated operational model was then applied to the second data set and the resulting pointing performance assessed with various terms refitted as might be done in a quick daily recalibration.

Operationally, the frequent observation of standard stars means there is an opportunity to adjust at least the boresight offsets more frequently, and this was simulated by allowing the terms IE and CA to float. They changed by (AEC/VertexRSI) 2.9/14.6 and 1.7/1.5 arcsec respectively and gave a sky RMS values of 2.44/3.05 arcsec, still somewhat outside the specification.

If the tilt terms AN and AW were allowed to vary in addition, the changes were (AEC/VertexRSI) 1.3/1.8 arcsec and 0.0/2.4 arcsec respectively, and the sky RMS values were 2.22/1.85 arcsec, somewhat better, and well within the specification for the VertexRSI antenna. This is an indication of the improvement that correctly working metrology (base tiltmeters) would offer.

With the azimuth zero point term IA added, completing the standard five floating terms, the sky RMS reduced only slightly, to 2.16 arcsec for the AEC antenna, and was unchanged for the VertexRSI antenna. However, a significant improvement in the fit to the AEC measurements, to 1.95 arcsec RMS, occurred when the Az/El non-perpendicularity term NPAE was included in the fit. The changes in the IA and NPAE terms for the AEC antenna were 11.2 and 12.6 arcsec respectively, and may be evidence of the suspected azimuth bearing instability in this antenna.

The conclusions are:

- Some form of rapid recalibration (say daily) will be needed in addition to any relatively infrequent full calibration.

- Frequent recalibration of the boresight offsets, IE and CA, is essential.
- Recalibration of the tilt terms, AN and AW, is also essential for the VertexRSI antenna performance, unless correctly functioning base tiltmeters can render this superfluous.
- Even with frequent recalibration of the boresight offsets, the AEC antenna performance would not quite reach the 2 arcsec specification.

6.3.7. Optical Tracking Tests on the VertexRSI Antenna

A pointing run consisting of observations of a single star for about 45 minutes was used to test antenna tracking performance. Because only a small region of sky was observed (a line about 10° long) the data set is not suitable for fitting a pointing model. Although doing so produces, it turns out, a sensible model, there is a danger of fitting out some of the tracking error that the experiment is designed to expose. Accordingly, an all-sky pointing run acquired during the following day was used instead. Applying this model to the tracking test and allowing only a zero-point correction (*i.e.* the TPOINT terms IE and CA) produced a sky RMS of 1.46 arcsec, and the $\Delta A \cos E$ and ΔE tracking residuals shown in Figure 18 (the x-axis is sequence number and hence time):

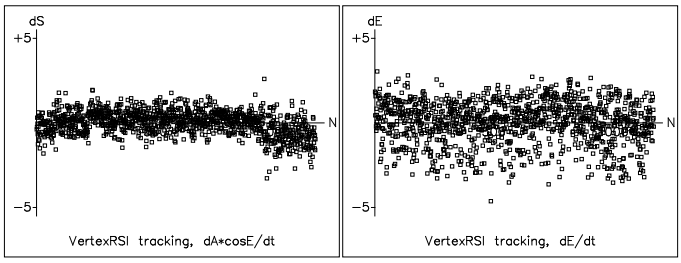

Fig. 18.— Tracking errors for the VertexRSI antenna. The x-axis is sequence number, and hence time.

Note that:

- The scatter up/down is larger than left-right, and is not normally distributed; the larger deviations tend to be downward on the plot.

- Beneath the noise, both axes show slow drifts. However, these are very small, barely 1 arcsec peak-to-peak. They might be the underlying errors in the pointing model, and how it varies from day to day and (if temperature plays a role) from hour to hour, or they could be anomalous refraction, or changing wind pressure. They happen too slowly to affect the ability to offset accuracy over short timescales, but do perhaps suggest that small adjustments to the pointing model on timescales of a few tens of minutes may be a wise precaution.

- The noise is of such high frequency that it is not what would usually be thought of as tracking error. This high frequency noise is more a "jitter", and is likely caused by the seeing-induced movements of the optical image, rather than the smoothness of the antenna motion.

- There is a fairly abrupt change in the left-right tracking near the end of the run, and hints of other relatively high frequency artefacts. If such events can happen during offsetting maneuvers the 0.6 arcsec in 2° science requirement might be in jeopardy. However, if the typical tracking were an illustration of the offsetting performance then the 0.6 arcsec figure would be easily achievable. In other words, in a typical 2° portion of the tracking plot the drift is within that figure. The largest slope on the elevation plot, for example, corresponds to about 2 arcsec in the total of 11° of track, or about 0.4 arcsec per 2°. The slopes on the $\Delta A \cos E$ track are, if we overlook the high-frequency events, somewhat steeper.

6.3.8. All-Sky Optical Pointing Summary

1. The rapid slewing of the ALMA antennas leads to data sets of ample size compared with the five or six variable terms of the model, and so the RMS figure is a good guide to the population standard deviation.

2. All-sky optical pointing measurements made over ambient temperatures from −10 to +20 C and during which the wind speed ranged up to 17 m/s showed no dependence on either of these site conditions.

3. For the AEC antenna, the all-sky RMS pointing accuracy from the 2004/03/06 through 2004/05/12 period (Figure 19) is typically 2.4 arcsec, with the better results in the first half of the test period, which was when the more stable IE and CA values were seen.

4. In Figure 19 the AEC sky RMS is resolved into two components, left-right and up-down respectively. It is evident that the left-right component (i.e. $\Delta A \cos E$) is worse

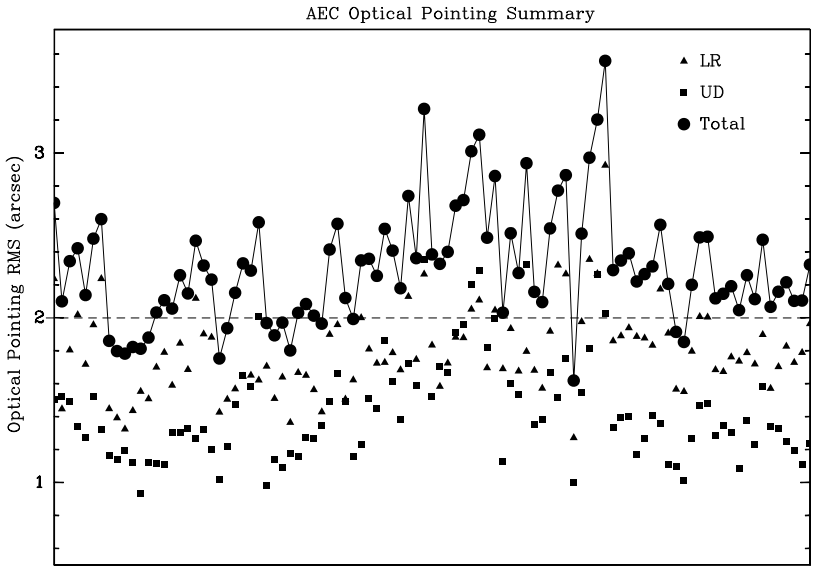

Fig. 19.— AEC antenna OPT all-sky pointing RMS. The horizontal, vertical, and total RMS are shown.

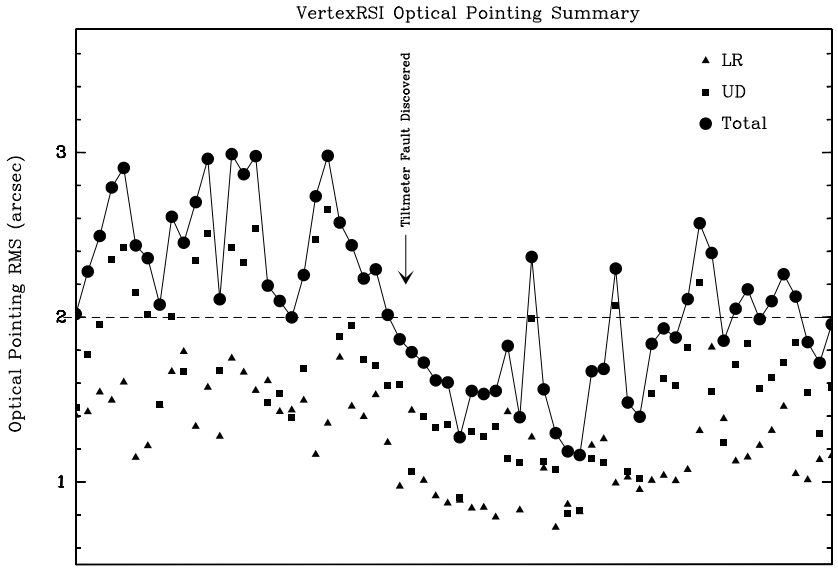

Fig. 20.— VertexRSI antenna OPT all-sky pointing RMS. The horizontal, vertical, and total RMS are shown.

than the up-down (i.e. ΔE) component. This worse azimuth behavior is fairly constant over the test period, whereas the unexplained decline in elevation performance in the second half accounts for most of the deterioration in overall RMS.

5. Figure 17 shows the AEC all-sky RMS pointing accuracy for the period 2005/01/07 and 2005/03/02. The mechanical modifications made by the antenna contractor have produced a moderate improvement to the all-sky pointing performance.

6. For the VertexRSI antenna, Figure 20 shows that if we neglect the earlier, pre-PMDR period, the sky RMS is not much affected by the passage of time and by changing conditions. A typical result is 2.0 arcsec RMS, and most of the PMDR runs delivered better than this, in some cases much better. Figure 20 also shows the sky RMS resolved into two components, left-right and up-down respectively. It is evident that the up-down component (i.e. ΔE) is worse than the left-right component (i.e. $\Delta A \cos E$). The performance variations in the two axes seem to be somewhat correlated, perhaps evidence that variations in optical seeing were involved, while the occasional poor sky RMS happened when there is a sudden worsening in elevation performance.

7. A sequential multiple star measurement, where each star measurement was repeated three times, was used to derive seeing and/or short timescale antenna positioning errors. These measurements suggest a seeing/vibration contribution of $\sim$1.5 arcsec, in line with the results from radiometric tracking tests. Extending the interpretation to account for the seeing contribution suggests that the true antenna pointing residual could be as low as 1.7 arcsec for the AEC antenna and 0.8 arcsec for the VertexRSI antenna.

6.4. Radiometric Pointing Measurements

Details of the radiometric test procedures can be found in Lucas, Mangum, & Matthews (2004). The radiometric data were logged in a different way from the OPT data and required some pre-processing, but the end results were similar in the two cases.

6.4.1. Radiometric Pointing Models and Results

Essentially the same procedure was used for both the OPT and the radio data. Special TPOINT scripts were used to mass-reduce the final selection of files, with automatic removal of outliers and with no manual intervention. The residuals from the different runs were

standardized and superimposed, first to look for hitherto undetected terms and then to determine the coefficient values for a fixed "core" group of pointing coefficients.

Radiometric pointing measurements were obtained during the period 2004/05/16-25 with the AEC antenna and 2004/03/20-22 with the VertexRSI antenna. Some pre-processing of the data was necessary before conventional TPOINT analysis could begin, to fold the operational model back into the observations. Once treated in this way, the four (AEC) and three (VertexRSI) measurement runs obtained, which contained (22, 30, 46, 57) and (44, 48, 37) pointing measurements, respectively, proved to be sufficiently consistent simply to concatenate them. Fitting each one separately was less promising given the relatively small number of observations in each data set.

For both antennas the first model tried was the OPT model with only IE, CA and HECE allowed to vary. The first and second terms are simply the radio boresight offset relative to that of the OPT. The third term is the Hooke's Law vertical flexure, which will be different for the radio and OPT cases. With this approach, the residuals were clearly systematic.

To deal with the elevation errors as a function of elevation, both HESE (elevation errors proportional to $\sin E$) and TX (elevation errors proportional to $\tan Z$) were tried, and the former worked best. This suggested some asymmetry in the BUS, subreflector supports or nutator.

There were also signs that the azimuth zero point correction (IA) and/or the Az/El non-perpendicularity (NPAE) had changed. The explanation (see §6.4.2) seems to be that the asymmetric location of the OPT, mainly in the horizontal direction, makes it vulnerable to elevation-dependent flexures in the BUS, a sideways deflection of the OPT occurring as the BUS "opens out" with increasing elevation. It was therefore decided to allow both of these terms to vary in addition to CA. For the AEC antenna these tests showed that a substantial 15 arcsec change in IA was needed, and an additional core term (HESE), but with no significant change in NPAE (under 1 arcsec in fact). For the VertexRSI antenna, only an 8 arcsec change in IA was needed, but large changes in HESE (46 arcsec) and NPAE (27 arcsec) were required.

With IA, IE, HESE, HECE and CA allowed to vary for both antennas (and for good measure AN and AW—these may change slightly depending on static wind pressure, and as they are rather uncorrelated with other terms are safe to include) satisfactorily non-systematic residuals were obtained. The final model obtained for both prototype antennas using this procedure is listed in Table 6.

For both antennas a plot of the $\Delta A \cos E$ and ΔE errors against observation number shows evidence of drifts during each of the pointing runs. For the VertexRSI antenna, the

Table 6: Radiometric Pointing Model

AEC			VertexRSI		
Coeff	Value	Sigma	Coeff	Value	Sigma
IA	−59.41	1.542	IA	−8.43	6.495
IE	+0.04	6.614	IE	−0.18	8.817
CA	+0.09	1.167	CA	+11.76	8.711
AN	+6.91	0.511	AN	−0.13	0.609
AW	−1.78	0.421	AW	−0.03	0.509
NPAE	+28.62		NPAE	+4.10	6.588
HESE	+17.84	5.230	HESE	+19.24	6.724
HECE	+40.63	4.882	HECE	+25.01	6.554
HASA2	−1.70		HASA	−1.20	
HACA2	+2.94		HACA	−4.42	
HESA2	−0.99		HASA2	+0.73	
HECA2	+1.53		HACA3	+0.38	
HVSA2	−2.25		HESA3	+0.94	
HVCA2	−2.08		HECA3	−0.34	
	Sky RMS = 4.35			Sky RMS = 4.77	
	Popn SD = 4.45			Popn SD = 4.94	

average drift for each of the three runs was just under 0.2 arcsec per observation. If the data from the three VertexRSI radiometric pointing runs are simply concatenated, without individual boresight adjustments, drifts in both $\Delta A \cos E$ and ΔE can be seen.

To derive the "best radiometric pointing model" from these measurements *without any drift corrections*, we used an analysis procedure similar to that used for the optical pointing measurement reductions. The HESE, HECE and NPAE coefficients were iteratively refined, and the individual pointing runs were normalized by freeing them from their preferred IE, CA, AN and AW values. The normalized data was then combined and then fitted for the five (AEC) and four (VertexRSI) core terms plus IA, HESE and HECE (and NPAE for the VertexRSI antenna). The resulting "best radiometric pointing model" for the AEC and VertexRSI antennas is shown in Table 7.

For each antenna its model was applied individually to each run by fitting only IE (plus drift), CA (plus drift), AN and AW and the results combined (Figure 21). The overall 3.2 arcsec and 5.3 arcsec RMS figures for the AEC and VertexRSI antennas, respectively, should be treated with some caution: superimposing individually fitted runs is a particularly optimistic way to present pointing results.

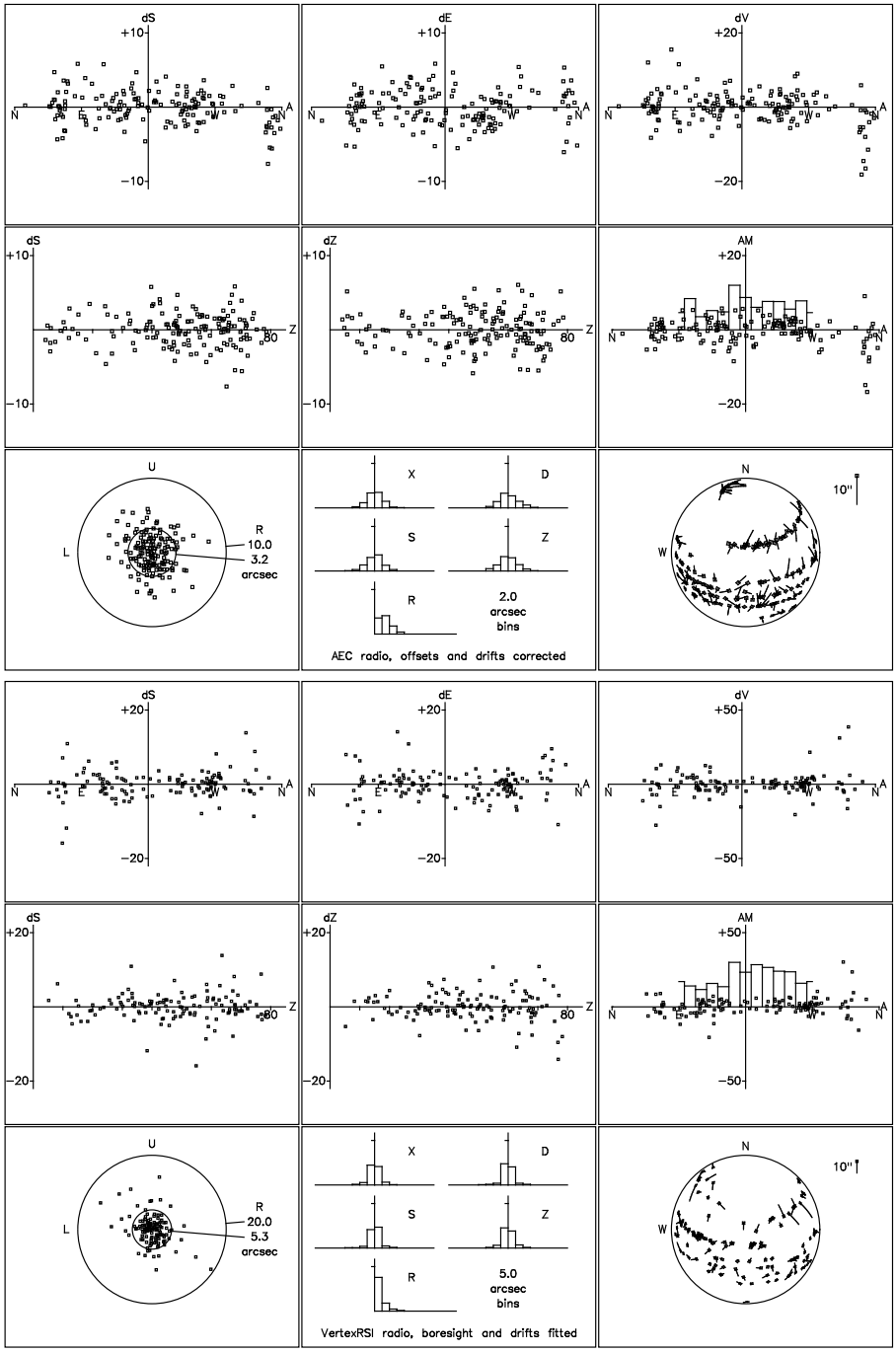

Fig. 21.— Superimposed best radiometric pointing model residuals for the AEC (top) and VertexRSI (bottom) antennas. See Figure 14 for a description of the quantities plotted in each panel above. The pointing model terms in this fit are listed in Table 7, which yielded an overall 3.2 and 5.3 arcsec RMS for the AEC and VertexRSI antennas, respectively. Note that these results are dominated by measurement error.

Table 7: Radiometric/Optical Pointing Model Comparison

AEC			VertexRSI		
Term	Radiometric	Optical	Term	Radiometric	Optical
IA	−59.41	−74.2	IA	−250	−258.0
IE	+147	−695.3	IE	+288	+433.0
CA	+273	−829.5	CA	+319	+173.0
AN	+6.91	+7.7	AN	−29	−31.0
AW	−1.78	−0.8	AW	+15	+14.0
NPAE	+28.62	+28.62	NPAE	+12.14	−15.01
HESE	+17.84		HESE	+17.95	−27.56
HECE	+40.63	−16.85	HECE	+23.16	+30.09
HASA2	−1.70	−1.70	HASA	−1.20	
HACA2	+2.94	+2.94	HACA	−4.42	
HESA2	−0.99	−0.99	HASA2	+0.73	
HECA2	+1.53	+1.53	HACA3	+0.38	
HVSA2	−2.25	−2.25	HESA3	+0.94	
HVCA2	−2.08	−2.08	HECA3	−0.34	

An analysis of the same three days of data was done (Lucas, Mangum, & Matthews (2004)) using the Plateau de Bure pointing model software. The results are in full agreement. No systematic effect was detected: the results are dominated by measurement errors.

6.4.2. Optical/Radiometric Pointing Correspondence

The location of the OPT within the backup structure of the antenna requires that one consider how the measurement axes of both systems are related. In the pointing model for the antenna concerned, for an ideal OPT fixed to the radio telescope surface and assuming mechanical symmetry about the axis of the parabola, one would expect only the boresight offset (IE and CA) and vertical flexure (HECE) terms in the pointing model to change. However, on both antennas, preliminary analysis of the radiometric pointing showed signs of the azimuth zero point correction (IA) and/or the Az/El non-perpendicularity (NPAE) having changed. The likely explanation of such effects is that the asymmetric location of the OPT, mainly in the horizontal direction, makes it vulnerable to elevation-dependent flexures in the BUS, a sideways deflection of the OPT occurring as the BUS "opens out" with increasing elevation. A deflection proportional to $\sin E$ would produce a term functionally identical to NPAE, while the $\cos E$ phase would produce an apparent change in IA.

For a perfect parabola at elevation 45°, the aperture of the antenna will change into being more elongated in azimuth at the zenith and more elongated in elevation at the horizon. Since the ALMA OPTs are located azimuthally off-axis, the boresight of the OPTs are expected to be pointed to more positive azimuths at the zenith, and to more negative azimuths at the horizon. One would expect, then, the following additional harmonic elevation and azimuth terms to the OPT pointing correction with respect to the radiometric pointing model:

$$
\begin{aligned}
\Delta E &= a \sin E \ \text{(same as HESE)} \\
\Delta E &= b \cos E \ \text{(same as HECE)} \\
\Delta A &= c \left(\frac{\sin E}{\cos E} \right) \\
&= c \tan E \ \text{(same as NPAE; equivalently a CA contribution proportional to } \sin E) \\
\Delta A &= d \left(\frac{\cos E}{\cos E} \right) \\
&= d \ \text{(same as IA; equivalently a CA contribution proportional to } \cos E)
\end{aligned}
$$

This indicates that one should expect fixed differences between the radiometric and optical determinations for IA, NPAE, HESE, HECE.

Taking the VertexRSI antenna as an example, a mechanical verification of this theory can be derived from the measured axial focus change due to BUS deflection (see Greve & Mangum (2006)). The VertexRSI BUS axial focus is measured to deflect by +1.7 mm over elevation range 0° to 90°. Using an 80% radiometric taper leads to a deflection of +1.35 mm. With the following constants:

$$
\begin{aligned}
x &\equiv \text{Distance from antenna axis to OPT} = 3494 \text{ mm} \\
f &\equiv \text{Antenna nominal focus} = 4875 \text{ mm}
\end{aligned}
$$

we find that, for a perfect parabola:

$$
\begin{aligned}
x^2 &= 2pz \\
\tan \alpha &= \frac{x}{2f} \\
\frac{\delta \alpha}{\delta f} &= 13.43 \text{ arcsec} \\
\delta \alpha (\delta \text{f} = 1.35 \text{ mm}) &= 18 \text{ arcsec}
\end{aligned}
$$

This corresponds well to the combined measured shift in NPAE ($+24''$) and IA ($-7''$) between our optical and radiometric pointing models for the VertexRSI antenna.

6.4.3. Radiometric Seeing

We have investigated the influence of refractive pointing errors (or "radiometric seeing") on our radiometric tracking measurements. Measurements of the differences between radiometrically-derived positions and their corresponding encoder positions while tracking a source for 15-20 minutes strongly indicate the existence of a refractive pointing error term (see Holdaway et. al. (2006)). These refractive fluctuations result in an ~ 0.6 arcsec radiometric positioning jitter. The magnitude of the inferred atmospheric pointing structure function at 1 s (the atmospheric crossing time of a 12 m antenna) is predicted to within 10% by theoretical arguments about refractive pointing jitter and Atmospheric Phase Interferometer data.

6.5. Optical Offset Pointing Tests

To investigate the accuracy of the offsetting performance, OPT observations were made where the antennas were switched repeatedly between a number of stars over distances of about 2°. Four (AEC) and seven (VertexRSI) such runs were conducted, consisting of 2 to 5 and 3 to 7 stars, respectively. The analysis of these observing runs proceeded as follows:

1. A fit and removal of the standard 13-parameter pointing model. In this model all parameters except the boresight offsets IE and CA were held fixed.

2. Outlier removal.

3. Concatenate the resulting files and perform a final fit to a model consisting only of the boresight position and drift terms IE, CA, A1S and A1E. This exhaustive removal of position and drift effects is appropriate here because we are investigating neither tracking nor all-sky pointing. The individual stars in the field are all equally affected by these measures, with any systematic effects associated with the transition from one star to another left as a residual.

4. For each star in this concatenated data set fit a model consisting of IE and CA alone. This last step reveals any systematic offsetting errors.

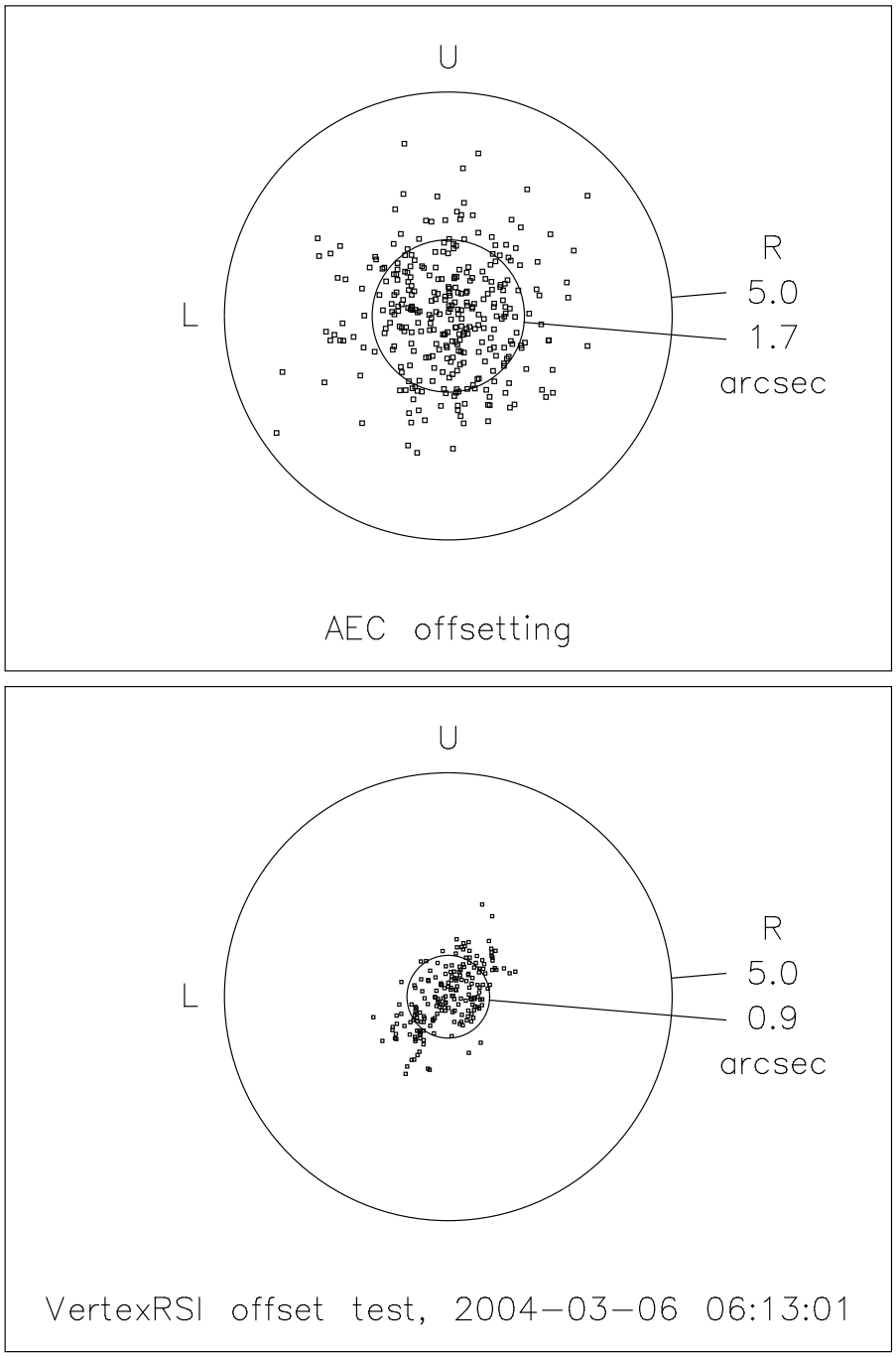

Fig. 22.— Sample AEC (top) and VertexRSI (bottom) offset pointing residuals.

The displacements of each star from the mean were then examined. Figure 22 shows sample offset pointing residuals for each antenna resulting from these analyses. The majority of the offset optical pointing runs for both antennas resulted in a derived offset pointing performance within the 0.6 arcsec specification. A couple of these optical pointing runs resulted in offset pointing residuals in the 0.9 to 1.1 arcsec range. These results appear to show that both antennas just miss the 0.6 arcsec offsetting specification. However, it must be borne in mind that not only were the experiments delicate and vulnerable to many sources of error, but also that the results were achieved without the metrology systems being active.

6.6. Metrology Performance

The AEC prototype metrology system originally comprised three components:

- Temperature sensor system to measure the pointing offsets due to thermal deformation of the structure.
- Tiltmeter system to measure pointing offsets due to tilts in specific structural elements.
- Laser interferometer system to measure structural changes in the fork arms of the antenna.

Only the temperature sensor and tiltmeter systems were installed on the prototype antenna. Attempts by AEC to qualify the temperature sensor and tiltmeter metrology systems were unsuccessful. The limited number of measurements that the AEG made with these metrology systems active lead to a poorer pointing performance for the antenna, which is a clear indication that these metrology systems were not functioning properly.

The VertexRSI antenna was designed to meet the pointing specifications with the aid of two separate metrology systems:

- A displacement sensor system mounted on the CFRP reference structure near each elevation encoder. This system was designed to measure the tilt component of the fork arm structure and BUS which cannot be measured by the encoders themselves.
- A system composed of two tiltmeters in the pedestal of the antenna. These tiltmeters are designed to measure the tilt of the azimuth axis.

Well into the evaluation the tiltmeter metrology system readout was found to drift by many tens of arcseconds over timescales of up to one minute. It was not clear what was

causing these drifts. This could be a problem with the software that applies these tiltmeter measurements to the antenna positioning, or to a mechanical problem with the mounting of the tiltmeters themselves. Once this problem was discovered, all pointing measurements were made with this metrology system disabled.

A number of measurements which included the corrections applied by the displacement sensor metrology system were made. Unfortunately, these measurements were not extensive enough to evaluate the effectiveness of the displacement metrology system. At the very least, this system did not make the pointing performance of the VertexRSI antenna worse.

We should note that even though none of the delivered metrology systems appeared to improve the pointing performance of either antenna, both antennas met the ALMA pointing specifications. Apparently the antennas on their own outperform their designed pointing performance specifications.

6.7. Evidence of Tripod Print-Through on the VertexRSI Antenna

To assess the viability of the low-level ($\lesssim$ 1 arcsec) terms in our pointing models we have checked the physical association of two of these minor terms with a plausible mechanical deformation on the VertexRSI antenna. The portion of the OPT pointing model involving $HESA3 = +0.94$ and $HECA3 = -0.34$ shows that the antenna nods in elevation as it rotates in azimuth, executing three cycles of nodding per turn of azimuth. This may be evidence of print-through from the tripod support into the azimuth bearing. The effect can be illustrated by removing all but those two fixed terms from the model, and then applying the model to a grid of stars all over the sky. The resulting plot of elevation corrections versus azimuth is shown in Figure 23.

The azimuths of the three pedestal legs would be aligned to the maxima of the nodding if there were no HECA3 term. The misalignment to the tripod leg positions is $\arctan(\frac{0.34}{0.94})/3$, or about 7°. The sign of the correction is such that when the antenna is pointing over a pedestal leg the star is about 1 arcsec higher in the sky than indicated by the elevation encoder reading.

To further confirm the mechanical interpretation of this $\sin 3A$ pointing term, measurements with the tiltmeter installed above the Az bearing were made at a slow speed (0.1 deg/s) and ±260° rotation in Az. These measurements show a single-angular sinusoidal response [$\sin A$] due to the inclination of the Az axis, and a three-angular sinusoidal response [$\sin 3A$] due to a repeatable wobble in the inclination of the antenna. The three-angular wobble is attributed to a wobble of the Az bearing. The three-angular wobble amounts to ±1.5 arcsec;

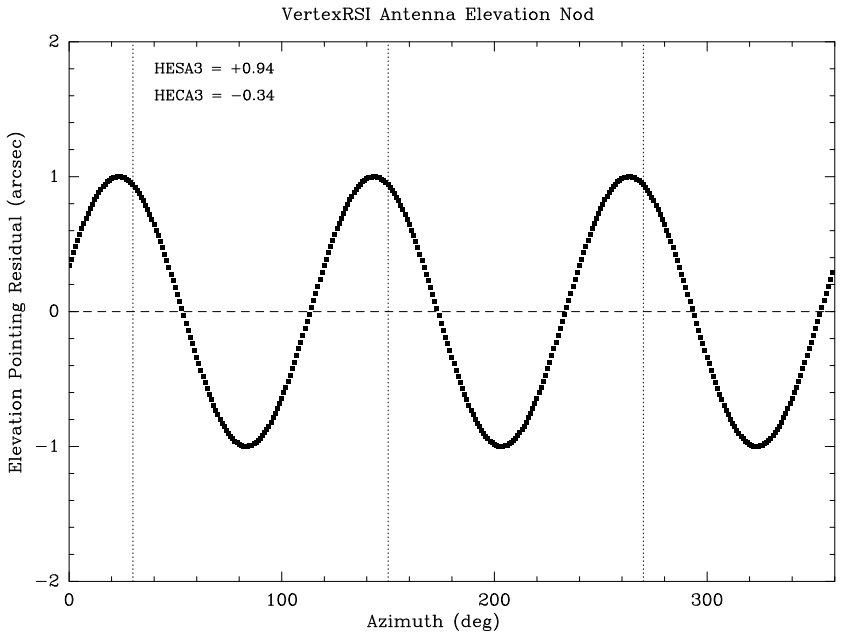

Fig. 23.— The HESA3 and HECA3 pointing model terms, showing possible tripod print-through in the azimuth motion of the antenna. The azimuth positions of the three mount points of the VertexRSI antenna are shown as dotted lines.

the extrema of the wobble are correlated with the location of the three-corner support of the pedestal. After elimination of the components $\sin A$ and $\sin 3A$, the residual deviation amounts to less than ± 0.5 arcsec (peak-to-peak).

The location of the extrema of the residuals from the $\sin A + \sin 3A$ fit is further evidence that the three-angular wobble is a print-through of the pedestal mount. The best-fit values to the measurement given by the following:

$$a0 + a1 \sin(A + b1) + a3 \sin(3A + b3)$$

are listed in Table 8 and shown in Figure 24.

We conclude that the telescope/azimuth bearing has a 3-Az wobble which seems to be very stable, and which is recovered and corrected for in the pointing model. The location of the 3-Az term suggests a print-through of the pedestal mount.

6.8. Accelerometer Measurements of Pointing Performance

The accelerometer system described in §5.3 and Snel et al. (2006) was used to derive three components to the antenna pointing performance:

- Cross-elevation pointing (left and right accelerometers on the rim of the BUS)
- Elevation pointing (top and bottom accelerometers on the rim of the BUS)
- Subreflector structure translations with respect to the BUS (four accelerometers on the rim of the BUS and one on the receiver flange).

Table 8: VertexRSI Azimuth Rotation Tilt Measurements

Parameter	2004 Feb 25	2004 Feb 25	Repeat 2004 Apr 10
Response	Linear	Linear + 3Az	Linear + 3Az
a1 (arcsec)	−32.9	−32.8	−31.2
b1 (arcsec)	56.659	56.811	59.912
a3 (arcsec)	...	−1.10	−1.13
b3 (arcsec)	...	−10.840	−4.638
RMS (residual) (arcsec)	0.85	0.30	0.25

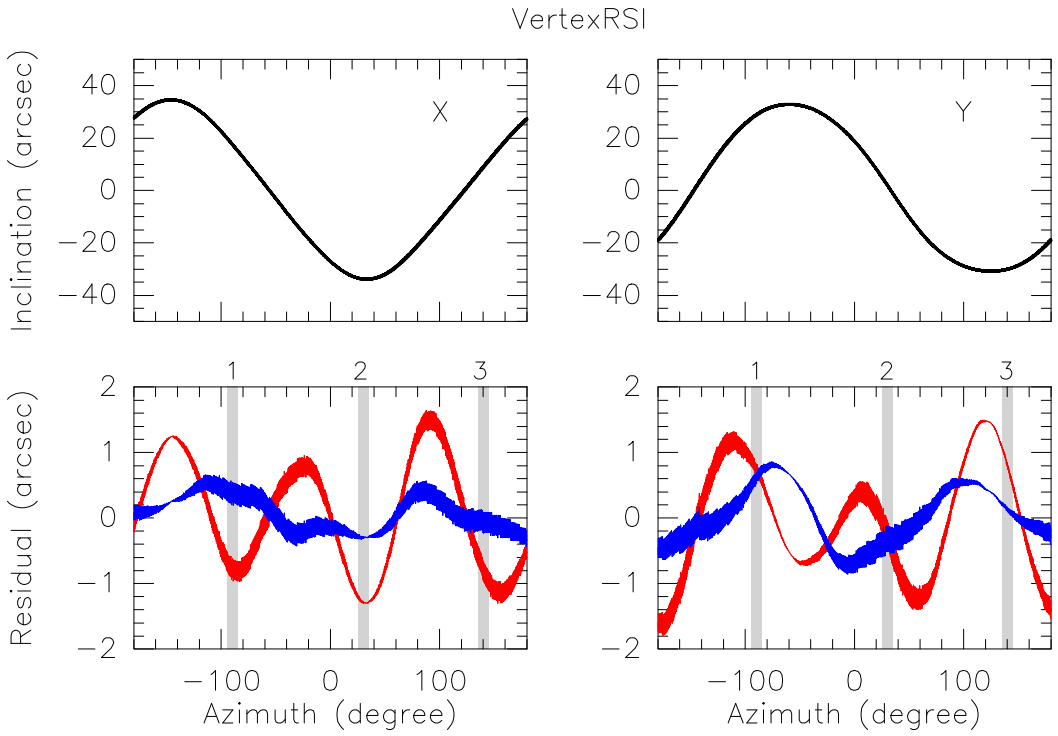

Fig. 24.— VertexRSI antenna measurement of -180^{o} to $+180^{o}$ AZ rotation. The left panel is the x–direction of the tiltmeter, the right panel is the y–direction. The red curves are the residuals of the best–fit $a_0 + a_1 \sin(A + b_1)$, the blue curves are the residuals of the best–fit $a_0 + a_1 \sin(A + b_1) + a_3 \sin(3\,A + b_3)$. The gray lines show the location of the pedestal corners (1,2,3).

In the following we characterize antenna pointing performance during several operational modes:

- Pointing toward a fixed (Az,El) without tracking (called "Stationary Pointing"). In this mode the drives are powered and the brakes are released. Wind effects are optimally investigated in this mode, as any effects of antenna shake due to position updates are minimal in this mode.
- Sidereal tracking. During sidereal tracking the antenna drives are constantly updating the azimuth and elevation positions, including the azimuth and elevation speed, in order to achieve a smooth tracking motion. Sidereal tracking was checked for 30 azimuth/elevation combinations spread evenly over the sky. Calm wind conditions were chosen, in order to clearly separate effects due to the drive system from those due to wind.
- Interferometric mosaicing and On The Fly (OTF) mapping at 0.05 and 0.5 deg/s scan speeds, respectively.

During the accelerometer measurements simultaneous wind speed and direction measurements were used to eliminate the effects of the local wind spectrum. Wind-related antenna performance was calculated for the same wind spectrum used for the design of the antennas. Our measurements provide us with the structural stiffness for wind excitation at frequencies between 0.1 and 3 Hz. We extrapolate from these to lower frequencies, using the low frequency component of the specified wind power spectrum to predict the pointing jitter due to wind for time scales up to 15 minutes (0.001 Hz). Because we could not measure the tracking jitter at these low frequencies, a conservative value equal to the observed tracking jitter at 0.1 Hz is used at 0.001 Hz as well.

The measured pointing errors under the various measurement conditions are assembled in Table 9. The cumulative errors as a function of frequency are shown in Figure 25 for the case of maximum wind (9 m/s) and scaled to the atmospheric situation at the final ALMA site at 5000 m altitude. As explained above, the section of the curves below the frequency of the asterisk has been extrapolated with the estimated constant value of the stiffness transfer function. Figure 26 shows a similar plot for the pointing jitter during sidereal tracking and low wind.

To supplement the information summarized in Table 9 we note that:

- For stationary pointing conditions under high wind loads the BUS rim wind shake is dominated by elevation motion for both antennas.

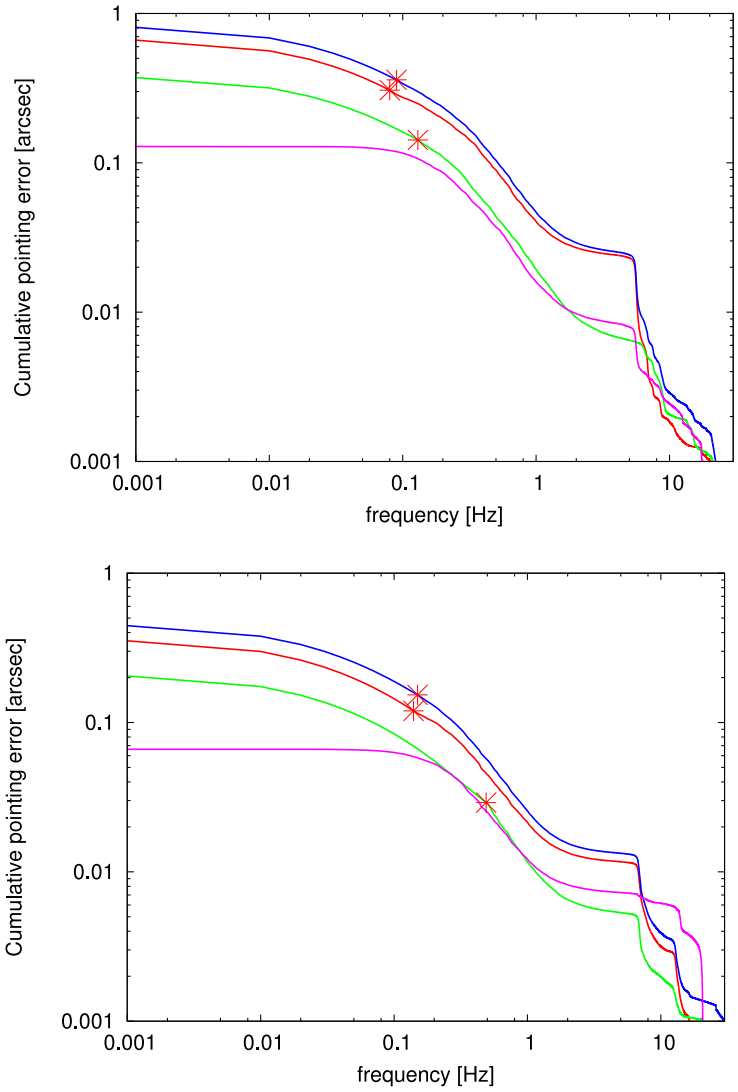

Fig. 25.— VertexRSI (top) and AEC (bottom) antenna cumulative elevation (red), cross-elevation (green), and total (blue) pointing error for extrapolated wind and Chajnantor pressure. The pink curve shows the cumulative encoder pointing error, which is totally dominated by elevation encoder errors. The asterisk shows the point below which the curve has been extrapolated to lower frequencies.

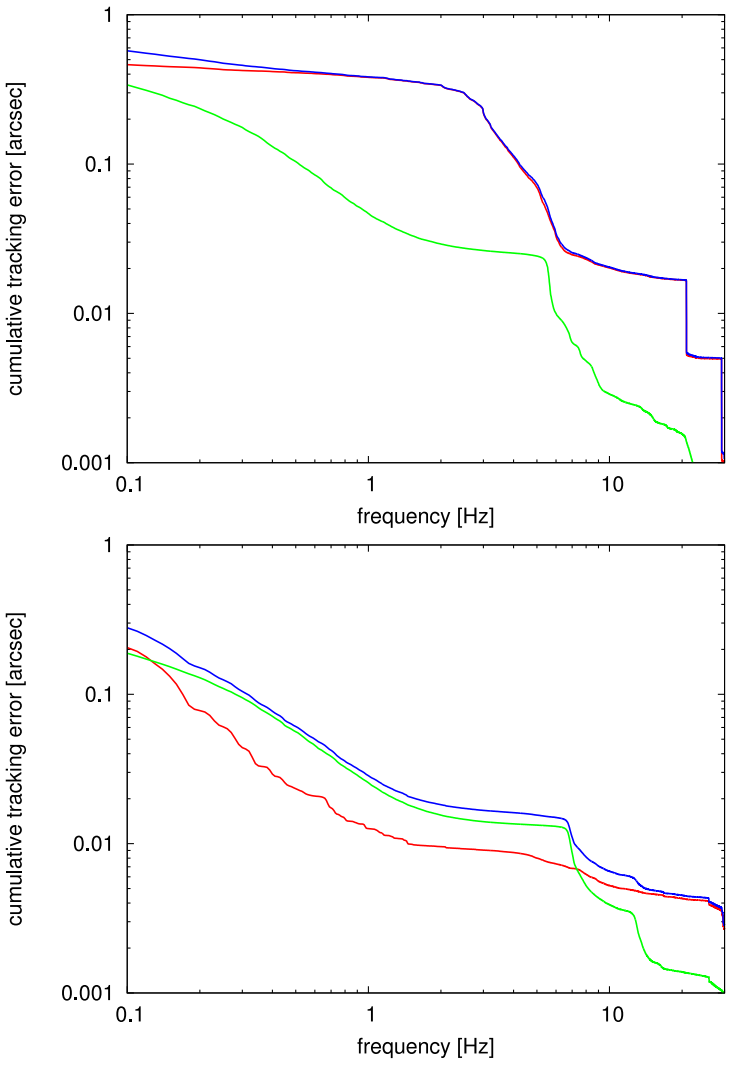

Fig. 26.— VertexRSI (top) and AEC (bottom) combined cumulative pointing error (blue curve) for wind (green) and sidereal tracking (red).

Table 9: Accelerometer Measurement of Pointing Errors

Measurement Condition	Δt (sec)	VertexRSI[a] (arcsec)	AEC[a] (arcsec)
Stationary Pointing (9 m/s wind)	900	$0.81 \pm 0.24 \pm 0.20 \pm 0.05$	$0.45 \pm 0.10 \pm 0.11 \pm 0.02$
Sidereal Tracking (no wind)	10	0.47 ± 0.11	0.22 ± 0.08
Tracking With Wind	10	$0.58 \pm 0.15 \pm 0.08$	$0.29 \pm 0.09 \pm 0.05$
Tracking With Wind	900	$0.94 \pm 0.26 \pm 0.20 \pm 0.05$	$0.50 \pm 0.13 \pm 0.11 \pm 0.02$
OTF at 0.5 deg/sec	1	1.7 ± 0.7	0.5 ± 0.3
Mosaicing at 0.05 deg/sec	1	0.8 ± 0.5	0.23 ± 0.01
Encoder Error[b]	900	0.14	0.07

[a] Contributions to each quoted value are defined, respectively, as pointing variation, spread, wind power spectrum uncertainty, and wind extrapolation uncertainty.

[b] The encoder error is included in the other values, but constitutes a small contribution.

- For sidereal tracking during low wind conditions the tracking jitter of both antennas is largely due to elevation motion, with large contribution in the 3-6 Hz range. Largest jitter is observed for low elevation, while minimum tracking jitter is seen while crossing the meridian.

- Assuming that the pointing jitter due to wind and that due to sidereal tracking are uncorrelated allows for the determination of the cumulative pointing error. A check of an independent measurement with high wind and sidereal tracking shows that this assumption is valid. Since no tracking jitter at 0.001 Hz could be measured, a conservative value equal to the observed tracking jitter at 0.1 Hz is used.

- For the VertexRSI BUS pointing stability during the fast (0.5 deg/s) OTF scan, the azimuth and elevation at which the scan is performed have large impact on the pointing stability during the scan, which is reflected in the standard deviation given.

- For the AEC BUS pointing stability during the fast (0.5 deg/s) OTF scan, pointing is affected for some parts of the scan by apex rotation feeding back to the BUS motion. This effect died out after a minute. The spread of 0.3 arcsec (1σ) reflects this variable pointing stability.

- The contribution of subreflector motion to the total pointing error has been investigated, but not included in the results presented here. This anomalous subreflector motion is due to excessive and off-axis rotation of the AEC antenna apex structure. Our accelerometer system measured only three degrees of apex motion, which did not allow for the separation of subreflector translation, which directly affects pointing, and

subreflector on-axis rotation, which has no impact on pointing. The results presented here are for BUS pointing only.

We would like to note that measurements of the dynamical behaviour of the antenna under operational conditions at this level of accuracy are extremely hard to perform radiometrically. The use of accelerometers for this purpose provides accurate results quickly and might be considered for routine checking of pointing stability.

6.8.1. Pointing Effects Due to Apex Motion

The apex structures of both antennas rotate about an axis that is assumed to be aligned with the boresight axis. However, for the AEC antenna, this axis is offset by −1.5 to +1.0 cm depending on the elevation. Fast switching can excite the rotation mode, which has translation components on-axis that can amount to 30μm peak-to-peak. The rotation and corresponding translation component is at 5 Hz, and damps out with a 1/e decay time of 5 seconds. With the prime focus plate scale of 34 arcsec/mm, this translates to radio pointing errors of up to 1 arcsec peak-to-peak in cross-elevation, provided that the rotation axis is parallel to the boresight axis, which could not be confirmed with the equipment available.

For the VertexRSI antenna, minor apex structure rotation was observed, which did not affect antenna performance since the rotation appears to be on axis.

6.9. Pointing Performance Summary

1. Due to the remarkably good pointing performance of both antennas, neither the optical nor radiometric tests offer sufficient resolution to tie down the performance of either antenna definitively, especially in the area of offset pointing.

2. The metrology systems were never properly commissioned and, in most cases, did not appear to work properly.

3. For the AEC antenna, the all-sky pointing is just outside specification, typically 2.2 arcsec RMS but with occasional 2 arcsec RMS results. The cross-elevation residuals are usually slightly larger than the elevation residuals, especially earlier in the test period when the elevation performance was particularly good. A sequential multiple star measurement was used to estimate the seeing and/or short timescale antenna positioning errors. These measurements suggest a seeing/vibration contribution of ∼1.5 arcsec,

in line with the results from radiometric tracking tests (see Holdaway et. al. (2004)). Extending the interpretation to account for the seeing contribution suggests that the true antenna pointing residual is 1.7 arcsec. This result should be weighed against the rather optimistic approach to the analysis presented in this document.

4. For the VertexRSI antenna, the all-sky pointing performance was typically 1.5 arcsec RMS.

5. The pointing model appears to be quite stable (exceptionally so in the case of the azimuth axis tilt terms) on the AEC antenna. Pointing model stability was measured to be adequate on the VertexRSI antenna. These measurements suggest that during operational use recalibration of each antenna (using perhaps four stars around the horizon and one near the zenith) every couple of hours would maintain peak pointing performance.

6. The offsetting performance of both antennas sometimes appeared to fall just short of the 0.6 arcsecond RMS specification for offsets of 2° or less, but this is a tentative result and not seen in all test runs. Given that the very stringent antenna specifications are a challenge that the measuring techniques struggle to meet, and taking into account the fact that the results were achieved without the help of the metrology systems, it is perhaps wise to return an open verdict on this aspect of the performance of the ALMA prototype antennas.

7. Using the accelerometers, the implied requirement of 0.6 arcsecond *tracking* stability in the offset pointing specification could be checked for sidereal tracking and wind shake. The VertexRSI antenna marginally misses this specification (0.94 arcsec RMS pointing stability over 15 minutes), while the AEC antenna was measured to be more stable at 0.50 arcsec RMS.

8. The wind-induced pointing jitter over timescales up to 15 minutes at 9 m/s wind was calculated in the antenna error budgets to be 0.035 (VertexRSI) and 0.35 (AEC) arcsec RMS. The accelerometers measured these values to be 0.81 (VertexRSI) and 0.45 (AEC) arcsec RMS, excluding the effects of subreflector motion.

9. OTF scanning at 0.5 deg/s lead to an average pointing stability over timescales of 1 second amounting to 1.7 arcsec RMS for the VertexRSI antenna, and 0.5 arcsec RMS for the AEC antenna. The specification is that the position is known at a given time, but the antenna does not need to point at the commanded position at that time. Measurements confirm that the pointing jitter as seen by the encoders matches that as derived from the accelerometers.

10. During interferometric mosaicing with rates of 0.05 deg/s, the commanded path is followed within 0.8 arcsec RMS for the VertexRSI antenna, and within 0.23 arcsec RMS for the AEC antenna. These are well within the specified value of 1 arcsec RMS.

11. The radiometric tests are too few for any firm conclusions to be drawn. At the frequency used, the beam width is about 1 arcminute FWHM, and the RMS result less than 10% of this, so there is no reason to suppose the underlying pointing and offsetting accuracy is poorer than the OPT measurements suggest.

7. Fast Switching

7.1. Optical Pointing Telescope Measurements of Fast Switching Performance

OPT offset and encoder data were used to compare the fast switching capabilities of the VertexRSI and AEC antennas. These fast switching measurements are performed by position switching between two stars that are bright enough to get high SNR position fits at the highest possible position switching rate (about 0.1 Hz). The optical pointing offsets as a function of time for each slew tell us how quickly the antenna can get on source and how quickly the pointing settles down after it gets on source. The optical pointing offsets include both mechanical antenna pointing and atmospheric "seeing" caused by dry air fluctuations (unlike in the radio, where the pointing jitter is caused mainly by water vapor fluctuations). Reasonable evidence that the encoders accurately reflect the antenna's mechanical motion is shown in Holdaway et. al. (2004). Hence, we expect that the encoder pointing offsets should also be very useful.

7.1.1. OPT Fast Switching Measurements

All OPT fast switching measurements were made on April 20, 2004. Four different star pairs were observed with each antenna. Two star pairs did not yield valid data for the AEC observations, while all four pairs of stars yielded good data on the VertexRSI antenna. Details of these observations are summarized in Table 10.

For each measurement run, the following analysis was performed:

1. The 20 Hz sampled encoder Az/El position information was linearly interpolated to match the corresponding 10 Hz sampled OPT Az/El star position information.

Table 10: OPT Fast Switching Measurements

Run	Antenna	t (UT)	Δt^a_{start} (s)	Az (deg)	El (deg)	$\Delta\theta$ (deg)	ϕ^b (deg)	SNR^c	σ^d_{atmos} (arcsec)
A	VertexRSI	6:07:46	1294	-258	63	0.4	-25	12	0.94/1.30/1.38
B	VertexRSI	6:30:32	998	-172	47	1.8	86	15	0.84/1.22/1.45
C	VertexRSI	6:52:42	1459	93	74	1.5	88	8	1.01/1.80/1.78
D	VertexRSI	7:18:52	680	110	22	1.4	5	8	1.40/2.02/1.44
E	AEC	7:43:08	552	-218	79	0.4	-2	18	0.34/0.33/0.97
F	AEC	7:52:38	553	-147	41	1.8	-71	16	0.64/0.57/0.89

[a] Duration of the measurement.

[b] Orientation angle of the vector joining the stars (0 degrees being horizontal).

[c] Signal-to-noise ratio cutoff used to determine star detection limit.

[d] Atmospheric pointing values are listed as Az component, El component, El-Az ratio.

2. Positions from the OPT Az/El data stream were identified as "target" (on-source) and "calibrator" (off-source) positions by assigning a star SNR cutoff to the OPT measurements.

3. Each target-to-target observation consumed about 5 and 4 seconds for the VertexRSI and AEC antenna measurements, respectively. Roughly speaking, the first ∼1.5 seconds are spent slewing to the source, the next second is spent refining the pointing, and the remaining time has a nearly stable pointing level.

4. The constant Az/El offset, representing the antenna pointing model, is removed from the OPT star position fits to derive the Az/El offset for each measurement.

5. For each run a single fourth order polynomial fit to the Az and the El encoder readings for the last half of all scans was subtracted from the Az and El encoder readings for that run to derive the RMS pointing errors.

6. For each slew, we are interested in the RMS pointing error as a function of the time since the last measurement from the previous slew. Time bins of width 0.2 seconds (twice the basic data sampling rate) representing the time from the end of the previous scan, and from the RMS of the Az and El offsets which fall into that time bin for all data in a 10-20 minute observation, were constructed.

7. Typically about 2% of the data points in each run were determined to be outliers and removed.

8. Optical RMS Az offsets, RMS El offsets, and the total RMS optical and encoder pointing errors as a function of time for each run and antenna were then derived. Figure 27 shows these results.

Comparing each run Az/El profile (see Figure 27), one sees general agreement, indicating that these two data streams are reliably aligned in time. However, the optical pointing RMS generally exceeds the encoder RMS pointing, as expected, as the optical RMS includes the effects of optical seeing. The optical seeing (σ_{atmos}) will be uncorrelated with the mechanical pointing errors, so it can be extracted from the optical pointing contribution by a quadratic subtraction:

$$\sigma_{atmos} \simeq \sqrt{\sigma_{opt}^2 - \sigma_{enc}^2}. \quad (1)$$

Table 10 shows the inferred atmospheric pointing contribution for each observation. In deriving these data, we considered optical and encoder data past the 2.5 second point in the profiles shown in Figure 27, calculated the inferred atmospheric optical pointing for each time bin, and took the average for all time bins past 2.5 second. Note that for the VertexRSI antenna, the ratio of El atmospheric pointing to Az atmospheric pointing is greater than 1.0, but for the AEC antenna it is about 1.0. We suspect that this is a further indication of the poorer elevation (VertexRSI) and azimuth (AEC) tracking and pointing performance noted in §6.

In conclusion, we find from our OPT measurements of fast switching performance:

- The VertexRSI antenna typically reaches its target source in 1.5-2.0 s.
- The VertexRSI antenna can have a significant pointing bounce in El between 2 and 3 seconds after the slew begins. Presumably, the servo is not well-tuned, and this is a correction for overshooting or something similar.
- The AEC antenna arrives at the target source after about 1.5 s, and has a much smaller pointing error after acquiring the source.
- The VertexRSI antenna has larger pointing errors after the source has been reached than the AEC antenna does, though the encoder data indicates that the specification of 0.6 arcsec is approximately met.

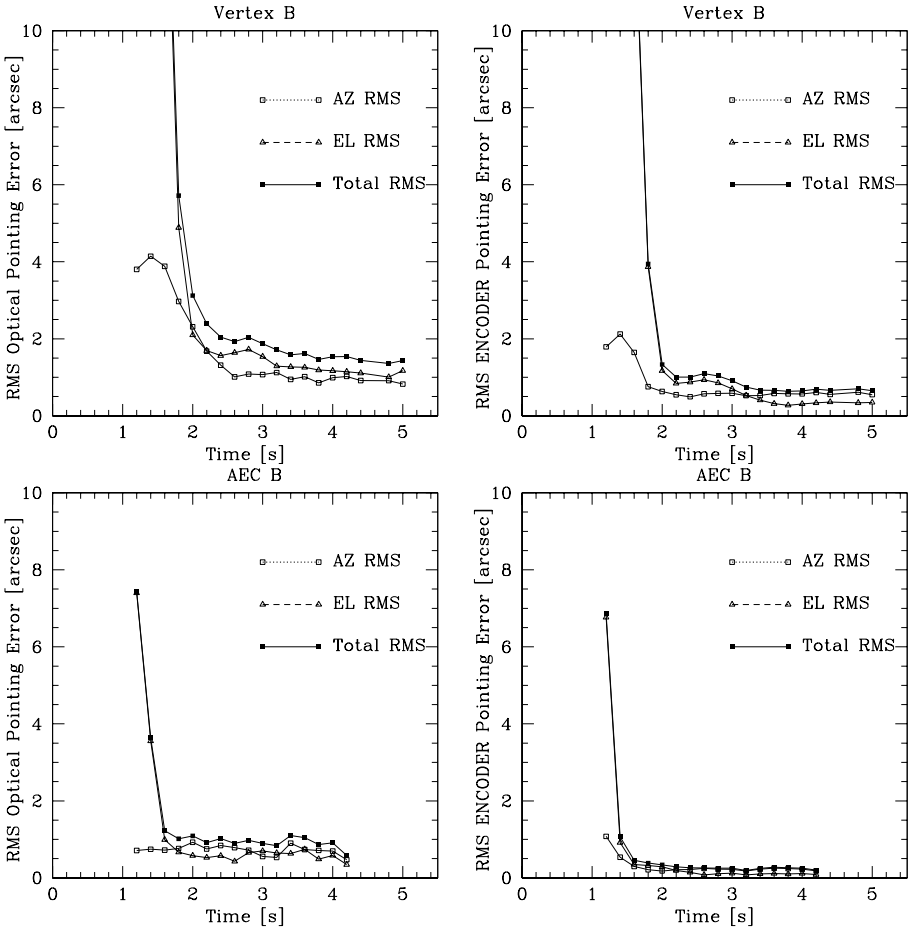

Fig. 27.— RMS optical pointing (left) and encoder (right) offsets as a function of time for a typical VertexRSI (top; Run B from Table 10) and AEC (bottom; Run F from Table 10) optical fast switching measurement.

7.2. Radiometric Fast Switching Measurements

We simulated radiometric fast switching interferometric observations by repetition of a blank sky integration, slew, then target source integration sequence of measurements. The blank sky integration simulates a fast switching calibrator measurement. The detailed sequence of measurements was as follows:

1. In order to see pointing fluctuations in both Az and El, we have performed observations with Jupiter at both its Az and El half power points (Table 11), and with a sequence of 21 antenna slews to the nearby "calibrator" (*i.e.* blank sky) of 1.5 deg in both Az and in El.

2. These total power measurements utilized beam switching to eliminate variable atmospheric emission with a subreflector throw of about 80 arcsec nutating at 10 Hz. The resulting differential total power measurements were found to be limited by gain fluctuations in our radiometric receiver system rather than incorrect cancellation of the atmospheric emission or thermal noise.

Table 11: Radiometric Fast Switching Measurements

Scan	Antenna	HPBW Offset	Switch Dir (deg)	El (deg)	TP_{on} (ampl)
5639	VertexRSI	El	+1.5 El	64.6	4.89
5640	VertexRSI	Az	+1.5 Az	64.5	3.08
5641	VertexRSI	Az	−1.5 Az	63.5	3.05
5642	VertexRSI	El	−1.5 Az	62.2	4.70
5643	VertexRSI	Az	+1.5 El	61.0	3.09
6759	AEC	Az	+1.5 Az	68.8	3.08
6762	AEC	El	−1.5 El	69.4	3.13
6767	AEC	Az	−1.5 El	70.0	3.08
6768	AEC	El	+1.5 Az	70.2	3.03

In summary, the analysis of these measurements proceeded as follows:

1. To calibrate the conversion from total power level to source offset we collected a series of three beam-switched total power measurements at offsets of +35, +40, and +45 arcsec from the half-power point of Jupiter. These data indicate the total power should change by about 0.160 for every arcsecond of pointing offset in the direction of the offset. In

the following we adopt this value for the change in total power versus position. The true scaling factor will be very close to this for the El scans, but the Az scans could have a scaling factor significantly different from this, *i.e.* as low as 0.11, which will increase the radiometrically inferred Az errors by as much as 50% due to uncertainties in the interpretation of the unmeasured peak flux for Jupiter. Note that the RMS of the 0.1 second data samples when OFF of Jupiter were typically 0.033. At 0.160 per arcsec, this indicates that the radiometer noise is equivalent to a jitter of 0.21 arcsec. Averaging for longer times can give us estimates of pointing errors with smaller uncertainties.

2. For each 0.1 second time stamp since the start of a slew (there are 20 slewing profiles going toward Jupiter per scan) we calculate the RMS of the measured total power minus the mean total power calculated from the last half of all 20 blocks in the scan, and divide by our calibration factor of 0.16 amplitude/arcsec. All 20 slew profiles within a given scan are then aligned and averaged to derive the radiometrically-inferred pointing error as a function of time, all shifted so they align with the slew that got on source fastest. A representative sample of these results is shown in Figure 28.

3. By averaging the approximately 500 samples made during the last-half of each scan a measure of the radiometric tracking accuracy, which includes contributions from the antenna and atmospheric fluctuations, was derived for the VertexRSI antenna. Typical values of 0.6 arcsec per axis, or about 0.8 arcsec total, were measured.

4. In the AEC antenna measurements we note that there is a 5 Hz oscillation in the positioning. This is a real mechanical effect because:

   - It has too much power at too small a time scale to fit with the atmospheric pointing error structure function,
   - It is seen in the encoder data (offset by 0.1 s),
   - It is not seen in the tracking data,
   - It seems to get excited as the telescope stops, and dies down with time (*i.e.* the telescope is settling down).

   The peak to peak of this positioning oscillation is about 0.4 arcsec. This oscillation has been identified as due to a mechanical oscillation of the apex structure (Snel et al. (2006)).

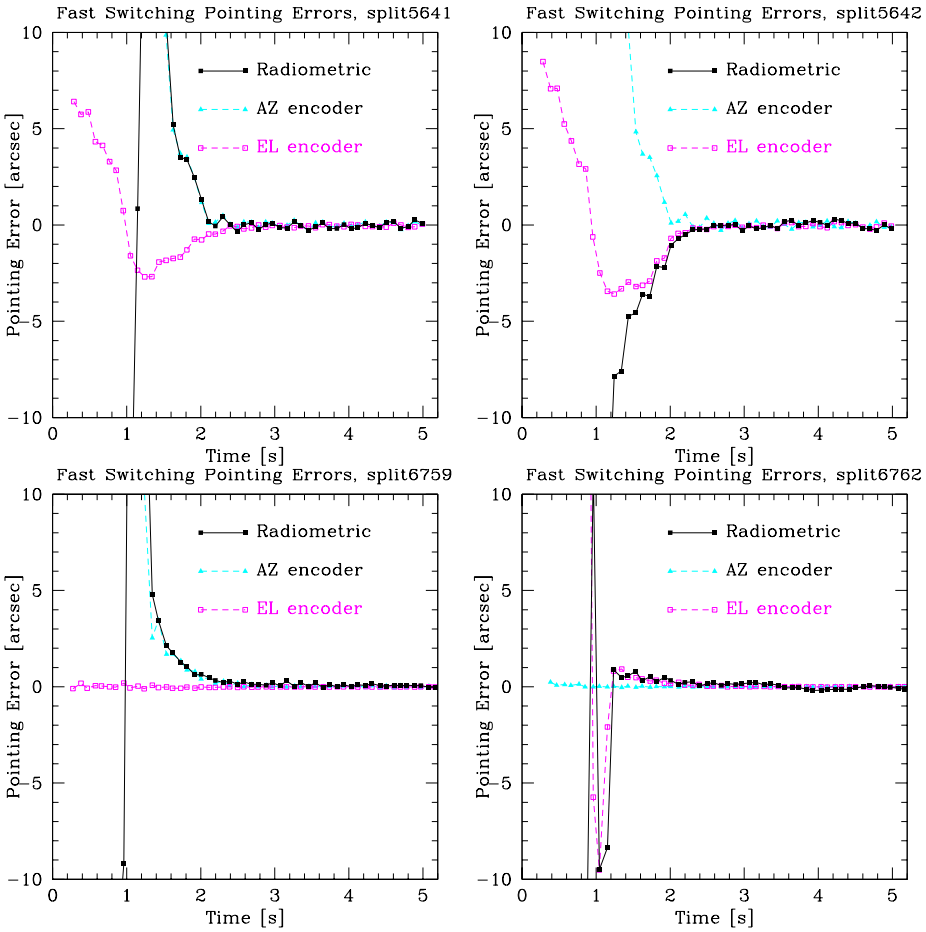

Fig. 28.— Radiometrically-inferred VertexRSI (top) and AEC (bottom) AZ (left) and EL (right) pointing errors for an AZ- and El-slew, respectively, along with encoder errors. The mean radiometrically-inferred (solid black) and mean azimuth (cyan dashed) and elevation (purple dashed) encoder pointing errors as a function of time since the start of the 1.5 deg fast switching slew are shown. Note that the noise level in these measurements is the time-weighted radiometric system noise of ~ 0.21 arcsec$/\sqrt{20} = 0.05$ arcsec.

7.2.1. Radiometric Fast Switching Performance Conclusions

Using radiometric and encoder data, we have investigated the mechanical aspects of the fast switching performance of the ALMA prototype antennas.

- The VertexRSI antenna basically meets the fast switching specification of "1.5 degrees in 1.5 seconds to an accuracy of 3 arcseconds". The antenna achieves pointing errors of about 0.8 arcsec RMS if a bit more settle time is permitted. Minor improvements

in the software and servo systems could improve the fast switching capability. We find that for night time observing, the encoders and the radiometrically-inferred pointing errors agree remarkably well. After the slew has been completed and the antenna is pointing on source, pointing drifts of under 1 arcsec over 2 seconds of time, and pointing jitter of amplitude 0.3 arcsec and frequency 3 Hz can be seen clearly in both the encoder pointing and the radiometrically-inferred pointing. On average, the encoders and radiometrically-determined pointing differs by 0.28 arcsec RMS while slewing and 0.15 arcsec after settling.

- Radiometric and encoder data from the AEC prototype antenna indicate that the AEC antenna meets the fast switching motion requirements. We see that as the AEC antenna comes to rest after a fast slew, a 5 Hz oscillation is excited by the fast switching motion, and that the peak amplitude of this oscillation is about 0.4 arcsec, which dies out over a few seconds. Accelerometer measurements have identified this oscillation as being due to a rotation of the apex structure (Snel et al. (2006)). For the measurements performed in this report, this oscillation does not prevent the AEC antenna from meeting the fast switching specification.

7.3. Encoder Measurements of Fast Motion and Settling Time

From the accelerometer measurements with comparison to the antenna encoder position information we gain an insight into the settling time after the fast position switch. We find that the VertexRSI antenna can perform a fast switch in the prescribed time and positioning limits, but not for all directions. There are no indications that the AEC antenna does not meet the fast motion and settling time specifications.

8. Path Length Stability

The path length stability of the antenna structures was measured using an Automated Precision Incorporated (API) 5-D laser interferometer (Greve & Mangum (2006)) and an accelerometer system (Snel et al. (2006)). In the following we describe the path length stability measurement results for both prototype antennas. Detailed descriptions of the technical capabilities of each measurement system are given in the associated references.

8.1. API5D Laser Interferometer Measurements

An Automated Precision Incorporated 5D (API5D) laser interferometer was used to measure the individual structural components that compose the total interferometric path length through the antennas. Laser interferometers are used to measure variations in "straightness" along a given path. One component of this "straightness" is the path length variation (Δ z). For the measurements made of the ALMA prototype antennas the accuracy in (Δ z) is better than 1 μm for an enclosed path, and 2 to 3 μm for an open–air path.

Since the total path length variation cannot be made with a single measurement, the total path length was separated into four parts (pedestal, fork arm, central receiver flange to subreflector, and subreflector to surface) and measured during a representative sample of observing conditions and operation modes. As shown in Figure 29, these measurements contain

L1: path length inside the pedestal = distance between the foundation (ground) and the lower face of the azimuth (AZ)–bearing; it was not possible to measure this path length on the AEC antenna;

L2: path length inside (one) fork arm (left, right) = distance between the lower part of the traverse and the upper part of the left (right) fork arm, below the elevation (EL)–bearing;

L3: path length along the radio axis = distance between the upper part of the Invar cone (VertexRSI), or the vertex hole (AEC, laser tracker mount) of the main reflector, and the apex of the subreflector; (in the measurements the dilatation of the aluminum subreflector support tube (50 cm length) has been eliminated, as far as possible;

L4: path length of the reflector = distance between the Invar cone/vertex hole and a point of the reflector surface, measured via the subreflector. On both antennas this path length measurement was tested but not routinely performed, mainly because of difficult alignment and time limitations. Since, in essence, this path length component originates in the CFRP part of the antennas, at least a temperature induced path length variation is expected to be small.

The full path length variation is approximately the sum of the measured components. Table 12 lists, while Figure 30 shows, the results from these path length stability measurements for both ALMA prototype antennas.

From simple geometrical and material arguments (thermal expansion coefficients), and the fact that wind forces act on short time scales, it was evident from the beginning that the

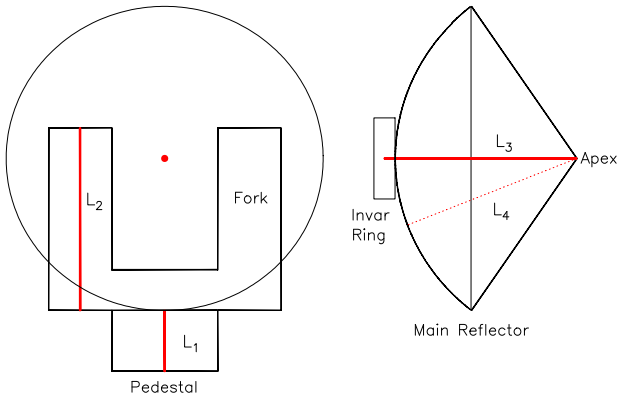

Fig. 29.— Illustration of the path length measurement scheme. Red lines indicate the path length sections measured with the API laser interferometer system.

Table 12: Path Length Variations Derived From API5D Measurements

	VertexRSI				AEC			
	3 min	10 min	30 min	Tot. Time	3 min	10 min	30 min	Tot. Time
Path	(μm)	(μm)	(μm)	(hr)	(μm)	(μm)	(μm)	(hr)
L_1 (pedestal)	3	6	10	250	∼5	∼5	∼5	Est.
L_2 (fork arm)	1.5	3	8	360	3	4	10	360
L_3 (quadripod)	5	5	5	25	4	5	∼10	25
L_4 (reflector)	∼5	∼7	∼9	Est.	∼5	∼5	∼5	Est.
Δ z	15	21	32	635	15	18	30	385

Note: Each measurement listed as averages over 3, 10, and 30 minute durations, along with the total measurement (or estimate) time, for each path.

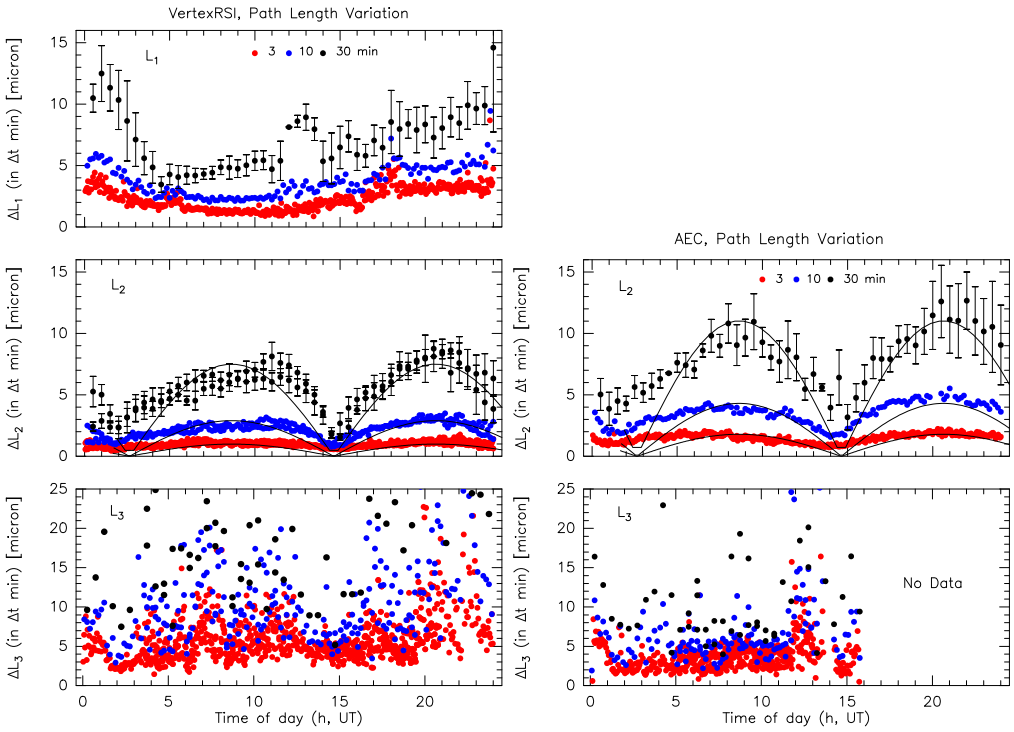

Fig. 30.— VertexRSI (left) and AEC (right) antenna path length summaries. Daily variation of path length L_1 (pedestal), of path length L_2 (fork arm), and of path length L_3 (Invar cone to subreflector), as function of the time of the day (UT), and within time intervals of 3 minutes, 10 minutes, and 30 minutes duration. Note the difference in scale. The black lines in the ΔL_2 panel are sine-function fits to the temporal variation in L_2, which track the daily ambient temperature variations at the VLA site (see Greve & Mangum (2006) for further information).

path length changes are, primarily, due to thermal dilatation of the antenna components, induced by variation of the ambient air temperature and solar radiation, buffered by the surface finish (paint) and thermal insulation. In the analysis of path length variations we have selected time intervals (Δ t) of 3 minutes, comparable to the time scale of wind, of 10 minutes, comparable to FSW (fast switch) and OTF modes of observation, and of 30 minutes, comparable to the time between upgrades of the pointing and interferometer phases. The data shown in Figure 30 were obtained during long time periods (listed in Table 12), and cover a large variety of antenna motions. For path lengths that could not be measured an estimated value is entered in Table 12.

In the following we investigate the path length dependence of both prototype antennas under a variety of the individual load conditions that went into the overall performance quoted above.

8.1.1. Path Length Variations Influenced by Temperature and Wind

For purposes of path length prediction, we have searched for correlation of the path length changes with the steel temperature of the pedestal and the fork arms, the ambient air temperature, and the wind speed. The correlation of the fork arm path length change ΔL_2 is shown for the VertexRSI antenna in Figure 31, and for the AEC antenna in Figure 32. As expected, the correlation of the path length change Δ L$_2$ with the change of the fork arm steel temperature is good, and usable for prediction. On the VertexRSI antenna, a similarly useful correlation was found for the path length of the pedestal (L$_1$; Greve & Mangum (2006)). There is no correlation between path length variation and ambient air temperature or wind speed variation.

A dedicated investigation of the path length changes with variations in wind speed was difficult due to logistical reasons. For one particular day, with changes of the wind speed (v) from $\sim$5 m/s to $\sim$15 m/s, the path length variation ΔL_2 (fork arm) of the VertexRSI antenna was measured, which hinted at a slight increase in ΔL_2 with increasing wind speed. However, the measured variation of L$_2$ remains within the specification even for the largest observational wind speed of v = 9 m/s. There are no data for the AEC antenna.

8.1.2. Path Length Predictions from Steel Temperature Measurements

Both prototype antennas have temperature sensors installed on the steel walls inside the fork arms. From these recordings we have derived the average, maximum, and minimum

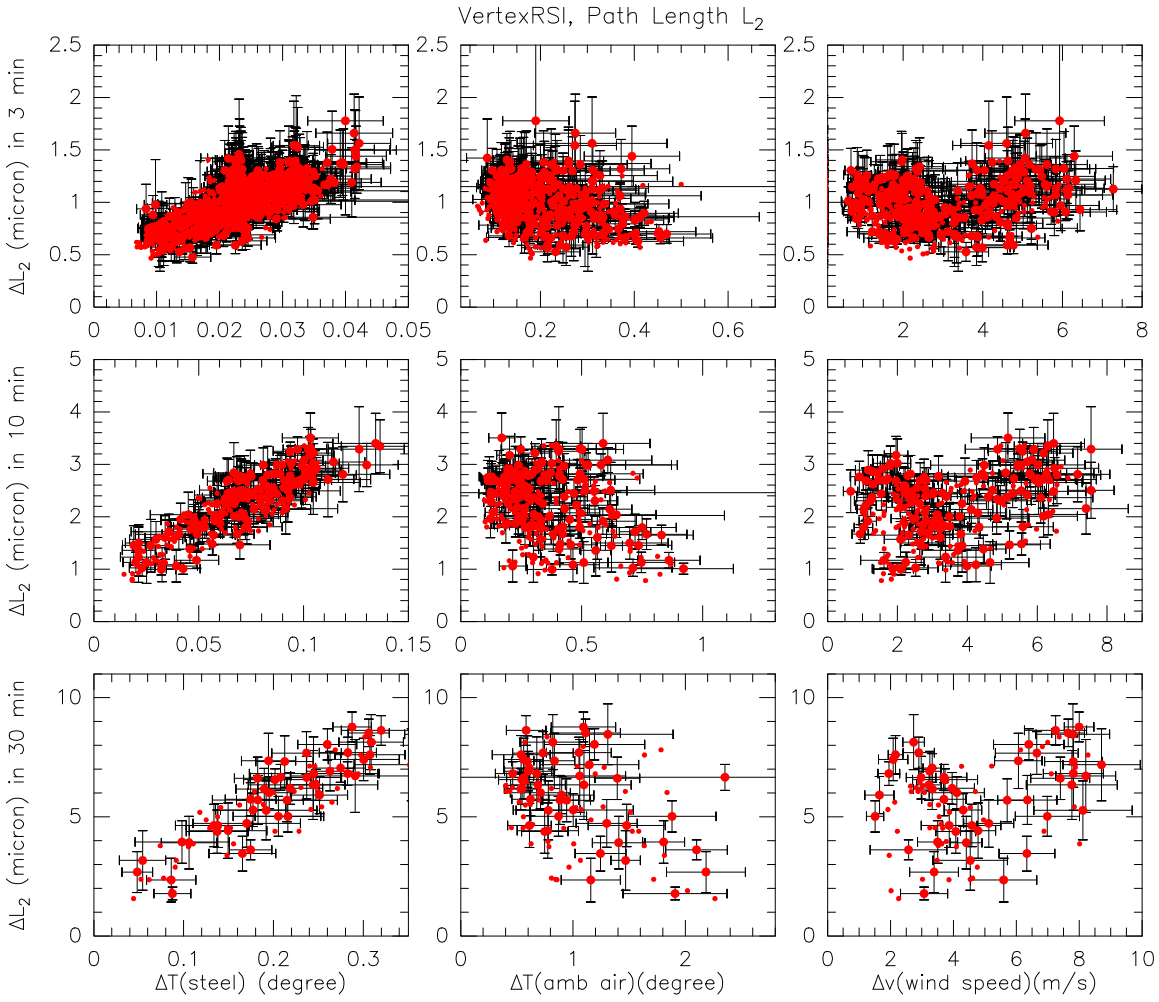

Fig. 31.— VertexRSI antenna dependence of ΔL_2 on the temperature variation of the fork [ΔT (steel); left] and ambient air [ΔT (amb air); center] and the variation of the wind speed [Δ v; right] for time intervals of 3, 10, and 30 minutes (top to bottom).

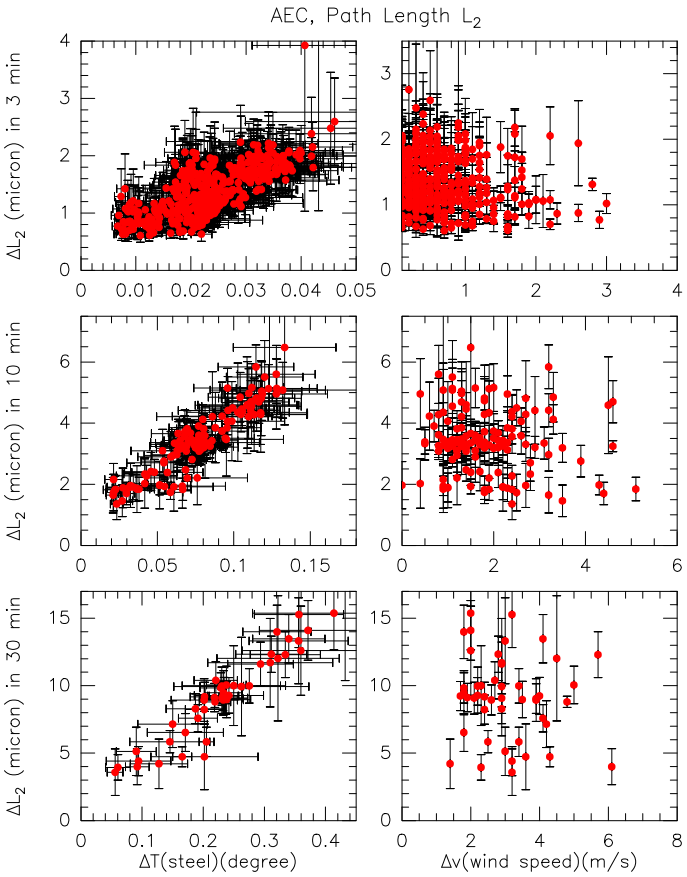

Fig. 32.— Same as Figure 31, but for the AEC antenna. Measurements of the ambient air temperature were not available.

temperature of each fork arm. The average temperature distribution measured throughout a fork arm was used in a finite element model (FEM) analysis to calculate the corresponding thermal dilatation $\Delta\,L_2$. Comparing the calculated thermal dilatation with the path length variation measured directly with the API5D, we find very good agreement as shown in Figure 33. From this we conclude that the path length variations of the steel parts can be predicted, to a high degree of accuracy, from representative temperature measurements used in the finite element model, or an empirical relation.

The daily temperature variation of the fork arms and the corresponding path length variation ΔL_2, both shown in Figure 33, can be approximated with good accuracy by sine–functions. This holds also for the ambient air temperature, at least as measured at the VLA site during most of the time of the tests. When adopting a sine–function $L_2(t) = L_o + \Delta L_2 \sin(\omega\, t)$, with $\omega = 2\,\pi/24\,h$ and t = time, the path length variation $\Delta\,L_2$ at a $3, 10,$ and 30 minute time interval can be derived by differentiation of the function $L_2(t)$. The corresponding result is shown by solid lines in Figure 33, which gives an explanation of the double peaked form of the measured variations. The minima of $\Delta\,L_2$ occur around 0^h and 14^h UT where the temperature changes of the ambient air and of the steel of the fork are smallest.

As is evident from Figure 33, the total daily path length variation of the fork arms is of the order of $100\,\mu$m to $200\,\mu$m, as fully understandable, and unavoidable, from the height of the fork arms, the thermal properties of steel, the actual temperature variation of the steel, and the solar illumination.

8.1.3. Path Length Variations During Antenna Motion

The ALMA interferometer will use sidereal tracking, OTF mapping, and FSW motions between source and calibrator. The OTF, and in particular the FSW motions, involve high accelerations of the antenna which may affect the path length stability. The path length variations ΔL_1, ΔL_2 and ΔL_3 were measured under the following motions of the antennas: (1) sidereal tracking, as a combined motion in AZ and EL direction; (2) OTF motion of 1^o AZ by 1^o EL, at 0.05^o/s); and (3) FSW motion of 1^o AZ by 1^o EL, at 6^o/s in AZ and 3^o/s in EL.

For both antennas, the variations of the path lengths L_1, L_2, and L_3 are within $\pm\,2\,\mu$m for sidereal tracking and OTF motion. For FSW motion, with the highest acceleration at the subreflector position of the quadripod, the path length measurements L_3 are shown in Figure 34. Again, for both antennas the path length variation ΔL_3 at the ON and OFF

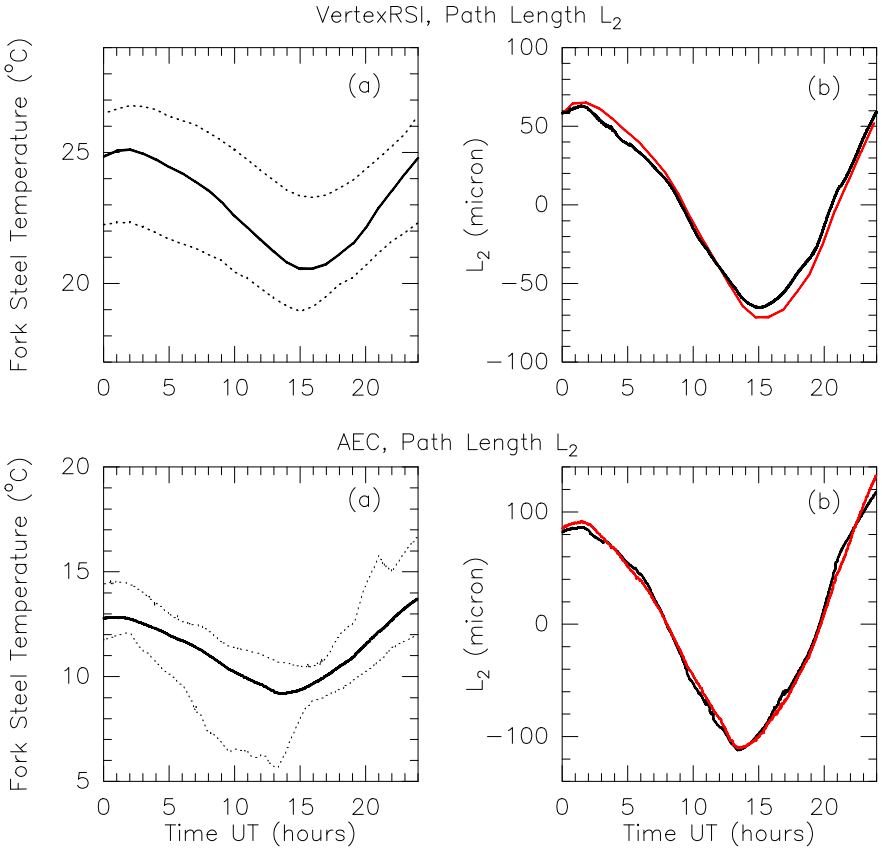

Fig. 33.— Correlation between the path length variation ΔL_2 measured with the API laser interferometer and FEM–calculated path length derived from the measured fork arm temperatures (14 sensors) for both prototype antennas. (a) Average (solid line) and maximum and minimum temperatures (dashed lines) of the fork arm steel derived from the 14 sensors. (b) Measured path length variation (black line), and that calculated from the FEM using the average temperature (red line). Similar results were obtained for other days.

position is within $\pm 3\,\mu$m.

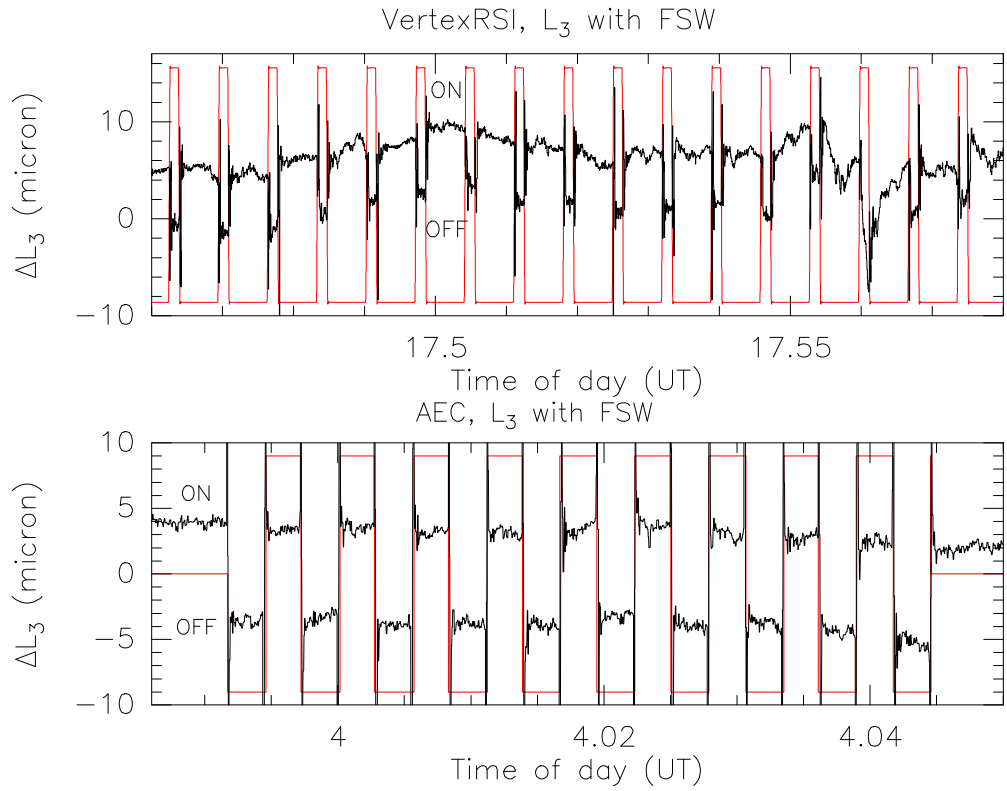

Fig. 34.— VertexRSI (top) and AEC (bottom) antenna path length variation ΔL_3 (Invar cone (VertexRSI) or reflector vertex hole (AEC) to subreflector) during fast switching motion. The switching cycle is shown by the red line, the path length changes by the black line. The ON (10 seconds for both antennas) and OFF (2 seconds for VertexRSI, 10 seconds for AEC) positions are indicated.

8.1.4. Influence of Gravity on L_3

Because of gravity induced deformations, on both antennas the path length L_3 will change with elevation of the reflector. To measure this effect, the laser emitter of the API5D was installed on a mount (specially constructed for the VertexRSI antenna; the laser tracker platform on the AEC antenna) at the reflector vertex, the retro–reflector was installed on the subreflector. The measurements of the L_3 path length variation as function of elevation are reliable because the measurements are insensitive to a small tilt of the laser mount relative to the antenna structure, and hence of the laser beam reflected in the retro–reflector. The antennas were tipped in elevation in steps of 15°, between 5° (AEC) or 15° (VertexRSI)

and 90° elevation, and the variation of $\Delta L_3(E)$ was recorded. These path length measurements, along with the path length variation predicted from a FEM calculation of the antenna structure, are shown in Figures 35 and 36. The repeatability of the API5D measurements is approximately $\pm 5\mu$m. Note that in Figure 35 the change in subreflector position as measured by the ALMA Antenna IPT using photogrammetry agrees well with the API measurement. Even though there may exist a difference between the measured and calculated variation of L_3 with elevation, the results indicate that the variation of ΔL_3 must be taken into account in the operation of the interferometer. They are easily put into analytic form.

8.2. Accelerometer Measurements of Path Length Stability

The accelerometer system described in §5.3 and Snel et al. (2006) was used to derive the *total* path length stability of the antenna. These measurements were derived from the four accelerometers on the rim of the BUS, one accelerometer on the receiver flange, and an accelerometer on the apex structure. The boresight motion of the BUS is subtracted from twice the boresight motion of the apex structure, which results in the total path length variation with respect to ground. As was done for the pointing results derived from accelerometer measurements (see §6.8) in the following we characterize antenna path length stability performance for the following situations:

Stationary Pointing in High Wind: Wind induced total path length variations for both antennas amount to 6 μm RMS over time scales of 15 minutes. These numbers are consistent with the path length stability as determined with the API5D instrument (§8.1 and Greve & Mangum (2006)). For antenna wake conditions path length stability is 11 μm RMS over 15 minutes.

Sidereal Tracking: For sidereal tracking, total path length variations over time scales of 1 second remain below 2 μm for the VertexRSI antenna, and below 0.5 μm for the AEC antenna.

Fast Motion: Total path length stability during fast OTF scans, with 0.5 deg/s scan rate, averages for the VertexRSI antenna to 12 μm RMS over time scales of 1 second. The AEC antenna path length stability averages to 3.3 μm RMS. When the scan rate is reduced to 0.05 deg/s for interferometric mosaicing, total path length stability of the VertexRSI antenna averages to 3.1 μm RMS over time scales of 1 second, and 0.7 μm RMS for the AEC antenna.

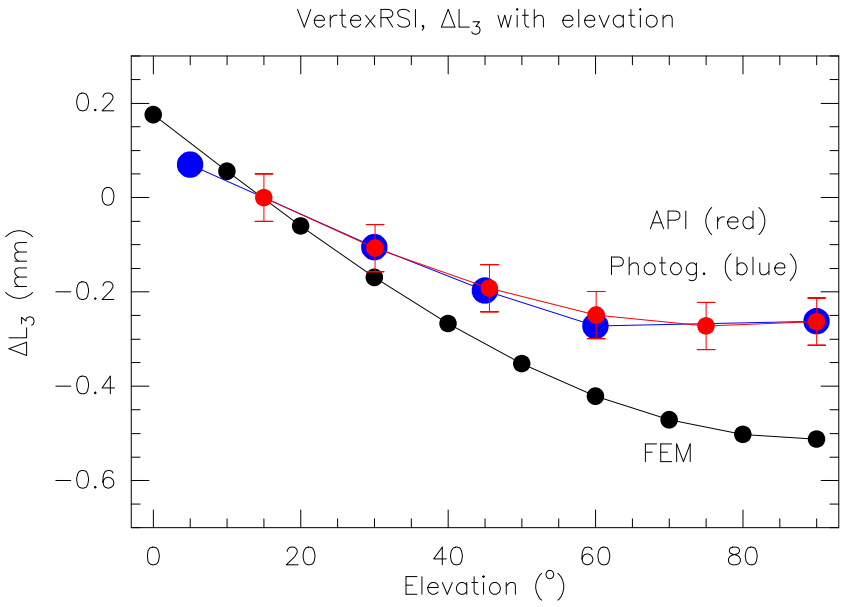

Fig. 35.— VertexRSI antenna. Path length variation ΔL_3 as function of elevation of the reflector, measured with the API and by photogrammetry. The curve indicated FEM is the calculated variation.

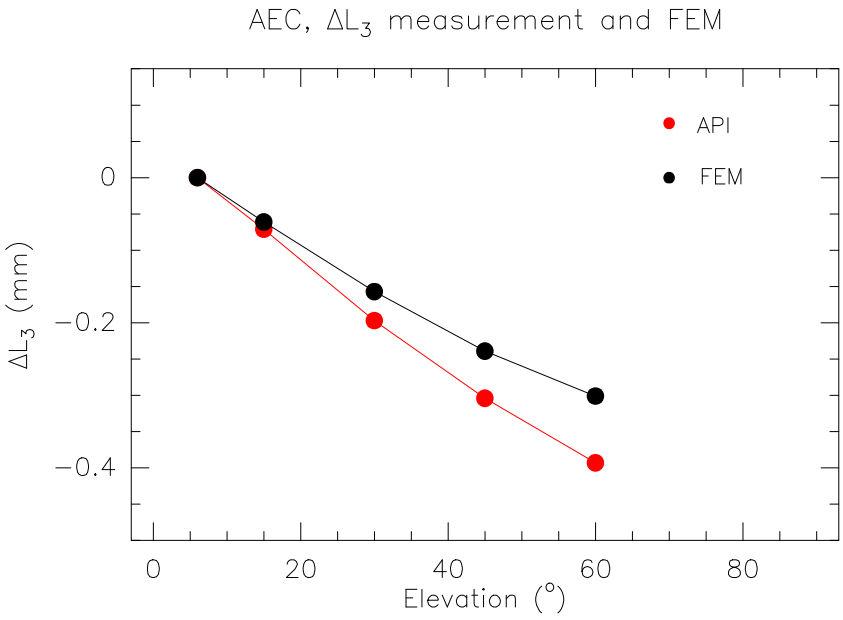

Fig. 36.— AEC antenna. Path length variation ΔL_3 as function of elevation of the reflector. The curve indicated FEM is the calculated variation.

9. Limitations of the Evaluation

In fulfilling its task the AEG was limited by a number of circumstances. Most importantly the atmospheric conditions at the VLA site did not allow the antennas to be tested at their highest operating frequencies. It is at the edges of the operational range where the antenna parameters can be most effectively determined by radiometric measurements. This formed the most serious limitation to our evaluation program. Instead, we have employed a number of optical-mechanical measurement devices in an effort to obtain sufficient material for a valid evaluation of the antennas.

Large delays in the delivery of the antennas shortened the evaluation process and limited the extent to which performance specifications could be tested. The VertexRSI antenna was marginally put at our disposal in March 2003, the AEC antenna in January 2004. Neither antenna was fully functional at those times. Summarizing, our ability to measure the full performance of the prototype antennas was limited in the following areas:

1. The holographic surface measurement was limited to one elevation angle. Some data on the reflector surface deformation as a function of elevation was obtained with optical methods.

2. The atmospheric conditions at the VLA site are quite different from those at the ALMA site on Chajnantor, Chile. Comparing the temperature and wind variations encountered at the VLA site with those at Chajnantor, it has been possible to draw meaningful conclusions regarding the behaviour of the antennas under the conditions specified for Chajnantor. However, at the VLA the atmospheric transmission only allows observations at the longer mm-wavelengths and over a limited (winter) period of the year. This has significantly impeded the quantity and quality of the radiometric tests. Moreover, we found that the VLA site has poor seeing - seldom better than 4 arcsec. This made the optical measurements of the important tracking and offsetting performance below 1 arcsec difficult to determine.

3. Radiometric pointing measurements are the final criterion for the determination of the pointing behaviour. The system temperatures of the evaluation receivers are excellent; however the limits set by gain fluctuations were factors of order 20 (at 3mm) and 10 (at 1mm) above the thermal fluctuations. Thus our limiting sensitivity was entirely set by gain stability at the 10 Hz switching frequency, restricting the number of available sources to $\sim$ 20 at 3mm wavelength. The nutator could only operate reliably under quiet or moderately windy conditions (a few m/s). Only a limited set of data could be collected at the VertexRSI antenna, and even less on the AEC antenna.

4. Some specifications fell outside our specific charter, in particular:

   (a) Time needed to remove and attach the antenna to its foundation.

   (b) Alignment errors after a drop of the antenna during transportation.

   (c) Mechanical and electrical requirements.

Considering these circumstances, it is gratifying to report that we were able to collect an amount of data that allows us to draw meaningful conclusions as to the performance of the ALMA prototype antennas. The test program on the VertexRSI antenna began in March 2003, but really useful data were collected only from October 2003 onwards. The AEC antenna program was started in January 2004. The entire program was concluded by the end of May 2004. Clearly, this time span did not allow us to make reliable statements on the long–term behaviour of the antennas.

10. Conclusions

The overall design and performance of the ALMA prototype antennas makes either of them attractive options for production antennas that will satisfy the stringent ALMA requirements.

Acknowledgements: The contributions of the following individuals were necessary for the success of the ALMA prototype antenna evaluation process: Marc Rafal (Commonwealth Technical Associates LLC); Fritz Stauffer, Nicholas Emerson, Jinquan Cheng, Jack Meadows (NRAO); Angel Otárola (ESO); José Lopez-Perez (OAN); David Smith (MERLAB); Michael Bremer (IRAM); and Henry Matthews (HIA).

REFERENCES

Baars, J. W. M., Lucas, R., Mangum, J. G., & Lopez-Perez, J., "Nearfield Radio Holography of Large Reflector Antennas", IEEE Antennas and Propagation Magazine, submitted

Emerson, D. T., Klein, U., & Haslam, C. G. T. "A Multiple Beam Technique for Overcoming Atmospheric Limitations to Single-Dish Observations of Extended Radio Sources", 1979, A&A, 76, 92

Greve, A. & Mangum, J. G., "Mechanical Measurements of the ALMA Prototype Antennas", IEEE Antennas and Propagation Magazine, submitted

Holdaway, M., Lucas, R., & Mangum, J. G., "Evaluation of Fast Switching and Tracking Performance of the VertexRSI and AEC Prototype Antennas using Radiometric, Encoder, and Optical Data", 2004, ALMA Prototype Antenna Evaluation Report Collection

Holdaway, M., Mangum, J. G., & Lucas, R., 2006, in preparation

Lucas, R., Mangum, J. G., & Matthews, H., "Radiometric Measurements of the ALMA Prototype Antennas", 2004. ALMA Prototype Antenna Evaluation Report Collection

Mangum, J. G., "The ALMA Optical Pointing Systems: Design Considerations and Prototype Description", 2004, ALMA Internal Report

Mangum, J. G., Baars, J. W. M., Greve, A., Lucas, R., Snel, R., & Wallace, P. T., "Evaluation of the ALMA Prototype Antennas", 2004, ALMA Internal Report Collection

Mangum, J. G. & Greve, A., "ALMA Test Facility Weather Instrumentation", 2004. ALMA Internal Report

Snel, R., Mangum, J. G., & Baars, J. W. M., "Study of the Dynamics of Large Reflector Antennas with Accelerometers", IEEE Antennas and Propagation Magazine, submitted

Smith, D. R., Avitabile, P., Gwaltney, G., Cho, M., & Sheehan, M., "Wind-Induced Structural Response of a Large Telescope", 2004, SPIE Vol 5495, pp. 258-26

Ukita N. & Ikeda M., "Antenna Vibration Measurements with Accelerometers", 2002, URSI GA (Maastricht)

Wallace, P. T., Mangum, J. G., & Lucas, R., "Evaluation of the ALMA Prototype Antennas: Pointing", 2004, ALMA Internal Report Collection